Nuclear Materials and Energy 45 (2025) 101983

Contents lists available at ScienceDirect

Nuclear Materials and Energy

journal homepage: www.elsevier.com/locate/nme

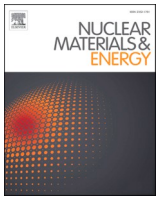

High heat flux testing of wire-based laser metal deposition coated plasma-facing components

Jannik Tweer [a,b,c,*], Thomas Derra [b,d], Daniel Dorow-Gerspach [a], Mauricio Gago [a], Sascha Gierlings [b], Stefan Gräfe [b], Gerald Pintsuk [a], Marius Wirtz [a], Christian Linsmeier [a], Thomas Bergs [b,d], Ghaleb Natour [e,f]

[a] Forschungszentrum Jülich GmbH, Institute of Fusion Energy and Nuclear Waste Management - Plasma Physics (IFN-1), Jülich 52425, Germany
[b] Fraunhofer Institute for Production Technology IPT, Aachen 52074, Germany
[c] RWTH Aachen University, Fakultät für Maschinenwesen, Aachen 52056, Germany
[d] Manufacturing Technology Institute MTI of RWTH Aachen University, Aachen 52074, Germany
[e] Forschungszentrum Jülich GmbH, Institute of Technology and Engineering (ITE), Jülich 52425, Germany
[f] RWTH Aachen University, Lehrstuhl und Institut für Schweißtechnik und Fügetechnik, Aachen 52062, Germany

ARTICLE INFO

Keywords:
Nuclear fusion
High heat flux (HHF) testing
Additive manufacturing (AM)
Wire-based laser metal deposition (LMD-w)
Surface regeneration
Tungsten (W)

ABSTRACT

The severe environment and loads acting on plasma-facing components (PFCs) of future fusion power plants cause inevitable erosion of their armor. In situ regeneration of tungsten (W) armored PFCs by local deposition of material would open up the possibility of damage healing and compensation of eroded material. The wire-based laser metal deposition (LMD-w) process fulfils the necessary requirements for use in the reactor vessel. Process development for the deposition of W on W substrate has already been carried out and it has been proven that thermal induced damage in the PFM can be healed this way. In this study, W armored PFCs were coated using LMD-w and tested under fusion–relevant thermal loads in the electron beam facility JUDITH 2. One respectively two stacked layers, each ~0.65 mm in height, were applied on the top surfaces of the W double tiles with surface areas of 28 × 12 mm^2 respectively, which are the characteristic dimensions for the plasma-facing surface of monoblocks. Some of the coated surfaces were also smoothed by laser remelting. In the electron beam facility JUDITH 2, the test components were exposed to steady state as well as combined steady state and transient thermal loads that are expected in the divertor area of the future DEMOnstration power plant. The coatings were tested with cyclic (200 and 1000 cycles) steady state thermal loading in the form of surface temperatures equivalent to heat fluxes on monoblock components of 10 MW m^{-2} (~1000 °C) and 15 MW m^{-2} (~1500 °C). To determine the performance of LMD-w layers under thermal loads that are expected during exposure to edged localized modes (ELMs), some layers were subjected to combined steady state and transient loading scenarios (0.13–0.55 GW m^{-2}, 10^3 to 10^5 pulses of 0.48 ms, 200–700 °C base-temperature). The temperature data obtained from the HHF experiments was processed and analyzed. Profile measurements on the coated surfaces before and after the high heat flux (HHF) exposure were used to investigate the influence of thermal stress on the deposited layers. Furthermore, cross-sectional micrographs of the test components were prepared and analyzed.

1. Introduction

For future fusion power plants (FPPs) it is planned to use deuterium and tritium (DT) as fuel [1]. During operation of large scale DT fusion reactors, the plasma–facing components (PFCs) and in particular the plasma–facing material (PFM) are exposed to demanding conditions [2]. Here, the plasma–wall interaction (PWI) processes include high particle fluxes in the form of plasma impinging on the inner wall, bombardment by high–energy up to 14.1 MeV neutrons and thermal loads [3]. The thermal stresses can be divided into steady state heat loads in the order of ~10 MW m^{-2}, which can reach up to 20 MW m^{-2} during slow transients (10 s with a limited number of 300 cycles), combined with extremely short transient heat loads in the GW m^{-2} range during edge-localized modes (ELMs) [2,4–8].

* Corresponding author at: Forschungszentrum Jülich GmbH, Institute of Fusion Energy and Nuclear Waste Management - Plasma Physics (IFN–1), Jülich 52425, Germany.
E-mail address: j.tweer@fz-juelich.de (J. Tweer).

https://doi.org/10.1016/j.nme.2025.101983
Received 15 July 2025; Received in revised form 26 August 2025; Accepted 5 September 2025
Available online 7 September 2025

Tungsten (W) is the most promising candidate for the plasma–facing material due to its high thermal conductivity ($\lambda \approx 120$ W m^{-1} K^{-1} at 1000 K), high melting point ($T_{melt} = 3695$ K), low sputtering yield and small tritium inventory [9–12]. However, even W suffers from several shortcomings in the context of fusion technology. These include the fact that only a minimal concentration of W is allowed in the plasma core (<few 10^{-5}) because radiation losses otherwise lead to excessive cooling of the plasma [13]. Furthermore, even if the plasma-facing material is made of a resilient element such as W, damage and erosion cannot be avoided, only mitigated [14]. As there is currently no reliable final design for the DEMO fusion reactor, it is not yet possible to provide precise information on the expected erosion rates. However, simulation studies carried out with the available DEMO fusion reactor parameters resulted in estimated divertor peak net sputtering erosion rates for W of up to 1.4 mm per full power year [15].

There are various ways to deal with the problem of the limited service life of PFCs. In order to keep the sputtering of W low, low plasma edge temperatures are therefore desirable [1]. But the plasma scenario can only be adjusted up to a certain point according to the stress limits of the PFCs if a high fusion performance shall be achieved. According to the current state of the art, entire PFCs are replaced by remote handling in DT machines such as JET and ITER when they reach the end of their service life or are critically damaged [16–19]. However, replacement of components in this way is an extremely resource–intensive procedure and results in massive reactor downtimes. For this reason, PFCs are currently designed to be as resilient as possible, and the armor layer is intentionally designed thicker to ensure that it can still fulfill its function even in the case of advanced erosion [20]. Increase of the armor thickness, on the other hand, raises the surface temperature of the PFCs, as the distance between the loaded surface and the coolant is increased [21]. So even with increased armor thickness, PFCs reach the end of their service life after a certain time in operation.

To ensure the competitiveness of future fusion power plants compared to alternative energy conversion technologies, it would be beneficial to explore alternative ways of dealing with damaged PFCs. One option is the repair of damaged PFCs to extend their service life. In order to prevent the time consuming replacement of components and thus keep the downtime of the reactor as low as possible, in situ repair is preferred over ex situ repair. Additive manufacturing (AM) processes from the direct energy deposition (DED) group could be used for in situ repair [22]. Powder–based processes only achieve maximum deposition efficiencies of ≤ 90 % and thus should be avoided for in situ operation to prevent contamination of the reactor chamber [23–25]. Accordingly, wire-based DED processes with near to optimal deposition efficiencies are more advantageous for this application [26,27]. For W, the wire-based laser metal deposition (LMD-w) process achieves deposition rates of up to 0.5 kg h^{-1}. Laser–based processes are advantageous, as the laser source can be positioned outside the vacuum vessel and the beam can be guided to the application site via glass fibers.

One approach is the in situ repair of PFCs by means of a robotic arm that is moved into the reactor vessel. There, the robot arm with its LMD-w processing head is planned to repair the damaged PFCs and compensates for erosion losses by deposition of new material. An LMD-w processing head (LMD-w-20-L) that can be stationed on a robot arm has already been developed [28].

It should be noted that such a concept using AM enables the repair and compensation erosion losses of PFM but is unable to repair damaged interfaces between the PFM and the structural material. The option of AM regeneration of PFM would also allow the design of thinner PFC armor, assuming that the PFM lost due to erosion could be reapplied by AM. Such reductions in armor thickness would lead to lower surface temperatures during thermal loading and thus to potentially higher resilience of the PFCs.

In previous studies, the deposition of W layers on W substrates by LMD-w was investigated [29]. Further, it was proven that thermally induced fusion–relevant damage to IGP W can be healed by deposition of LMD-w W coatings on small W–samples or remelting the substrate with a laser [30]. In this study, the behavior of LMD-w W coatings in ITER–like monoblock dimensions is investigated under the thermal loads expected for the PFM of high power nuclear fusion reactors. As part of this study, various coatings were applied to the surface of W–armored test components using LMD-w. These coatings were applied in accordance with the findings obtained in previous studies on the coating of W substrates with LMD-w W [31]. The aim of the subsequent thermal exposure experiments is an evaluation of the performance of the LMD-w W coatings under fusion–relevant thermal loads, that are expected in future FPPs. So, the LMD-w coated test components were subjected to fusion–relevant steady state as well as combined steady state and transient thermal loads in the electron beam facility JUDTIH 2 [32–34]. During the high heat flux (HHF) experiments, temperature data was obtained using pyrometry and IR imaging, which was later analyzed. Profile measurements of the loaded W surfaces before and after HHF exposure were subjected to detailed analysis. Cross-sectional micrographs were prepared to obtain insight into the bulk material after exposure to thermal loading.

2. Experimental

2.1. Test component development

To determine the performance of LMD-w regenerated PFCs under thermal conditions at the divertor of future fusion power plants (FPPs), HHF exposure studies were conducted. Actively cooled W armored test components are required to perform these experiments. As it was not possible to obtain entire monoblock chains for these early stage experiments and manufacturing in–house is not feasible, an alternative test component design had to be developed. The selected flat tile test component design is illustrated schematically in Fig. 1 in the cross section B.1) and isometric view B.2) alongside an ITER-like divertor PFC (monoblock chain) design with the cross section A.1) and isometric view A.2) [5,35,36]. The flat tile design was chosen to manufacture the

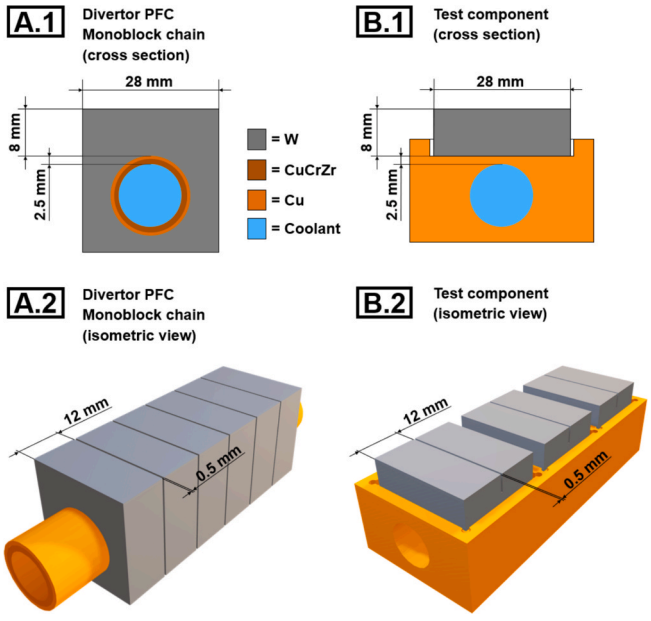

Fig. 1. The divertor monoblock chain design is schematically illustrated in the cross section A.1) and isometric view A.2). The test component design for the HHF experiments is illustrated in the cross section B.1) and isometric view B.2). For both designs, the W surface area for thermal loads acting from above is 28 × 12 mm^2. In both variants, the thermal energy arriving from the top surface has to be conducted in the center of the component through 8 mm W and 2.5 mm Cu/CuCrZr to reach the coolant.

components without the hot radial pressing (HRP) process, which is one option for manufacturing of monoblock chains [37,38]. The test components were designed with the aim of subjecting the W coatings deposited by LMD-w to thermal conditions as similar as possible to those on real PFCs. The thermally loaded W surface area for both components is 28 × 12 mm^2 per monoblock or half of a W double tile (Fig. 1A.2) and B.2)) [5,35,36]. During HHF exposure, the thermal energy arriving from above has in both cases (compare Fig. 1A.1) and B.1)), to be conducted through 8 mm of W and 2.5 mm of Cu/CuCrZr. Thus, the heat transfer in the test components is comparable to those of monoblock components. Accordingly, during the HHF experiments of the test components, similar thermal conditions (including temperature gradients) can be created for the LMD-w layers, as on the real monoblock components. However, this only applies perfectly to the part of the test component located centrally above the cooling channel, since the edges of the W tiles are slightly cooler than those of monoblocks during thermal loading due to the larger copper part (comparing the cross sections in Fig. 1A.1 and A.2). For monoblock chains, the distance between two neighboring monoblocks is 0.5 mm (Fig. 1A.2)) [35]. To test whether the deposition of W by LMD-w can be performed precisely enough to maintain this gap, W double tiles were produced. These W double tiles contain two tiles, which are connected to each other at the lower side by 3 mm thick bulk material, thus ensuring a defined distance of 0.5 mm between each other. These double tiles are visible in the isometric view of the test component design in Fig. 1B.2). To test the performance of the LMD-w layers under fusion–relevant HHFs, several W double tiles were designed to heights of only 7 mm, so that the missing material to reach ~8 mm can be achieved by LMD-w deposition of W.

Table 1 lists the calculated surface temperature ranges at the plasma-facing surface of ITER divertor components (Fig. 1A)) when exposed to fusion reactor–relevant steady state heat fluxes. In the following HHF experiments, LMD-w coated test components were exposed to temperatures equivalent to those experienced by divertor components during fusion reactor operation. To ensure that not only the surface temperature but also the temperature gradients within the components are adequately reproduced during these experiments, the test component is actively cooled. Active cooling is also necessary to dissipate thermal energy and prevent components from overheating. To simplify manufacturing and assembly, no swirl tape inserts were used [5]. Apart from that, the cooling parameters are similar to those used to cool monoblock chains. Table 2 lists these cooling parameters of the sample cooling circuit of the electron beam facility JUDITH 2, which were used in these HHFs experiments. The selected coolant is purified water.

The thermal behavior of the test components during the loading procedure was calculated using finite element method (FEM) simulations performed with Ansys 2020 R1 software. In this way, valuable information was obtained prior to the physical experiments that enabled the desired thermal loading scenarios to be precisely configured. For these FEM simulations the convective dissipation of thermal energy on the inner surface of the cooling channel of the test components, driven by the cooling water, was calculated using a Nukiyama code developed by ITER with the parameters listed in Table 2.

Here, the convective heat transfer coefficient at the surface of the cooling channel h_{cv} [W m^{-2} K^{-1}] is calculated as follows [39]:

Table 1
Calculated temperature ranges at the plasma–facing surface of actively cooled ITER divertor monoblocks when subjected to the respective steady state heat fluxes [21].

Heat flux	Temperature ranges
10 MW m^{-2}	950–1058 °C
15 MW m^{-2}	1411–1612 °C
20 MW m^{-2}	1864–2146 °C

Table 2
Coolant parameters used during the HHF experiments in the electron beam facility JUDITH 2.

Cooling parameters	Symbol	Value	Unit
Fluid temperature	T_f	70	°C
Fluid velocity at the input	v_f	7.5	m s^{-1}
Fluid pressure at the input	p_f	4	MPa

$$h_{cv} = Nu\frac{\lambda}{D_h}\left[\mathrm{W\,m^{-2}K^{-1}}\right] \tag{1}$$

where Nu is the dimensionless Nusselt number, λ the fluid thermal conductivity [W m^{-1} K^{-1}] at film temperature, and $D_h = 4A\ p_w^{-1}$ the hydraulic diameter [m]. In this context, A represents the cross–sectional area [m^2] of the cooling channel and p_w is the wetted perimeter [m]. The Nusselt number describes the ratio of convective and conductive heat transfer. It can be approximated by various heuristics [40,41]. Here, the Sieder–Tate equation was utilized to calculate the Nusselt number [42]:

$$Nu = 0.027Re^{\frac{4}{5}}Pr^{\frac{1}{3}}\left(\frac{\mu_{db}}{\mu_{dw}}\right)^{0.14} \tag{2}$$

where Re is the dimensionless Reynolds number and Pr is the dimensionless Prandtl number. μ_{db} represents the dynamic viscosity of the fluid at bulk [kg m^{-1} s^{-1}] and μ_{dw} its dynamic viscosity [kg m^{-1} s^{-1}] at wall temperatures. In general, the Reynolds number Re is used to describe the flow characteristics of fluids. The higher the Reynolds number, the more turbulent the flow. The Reynolds number Re is the ratio of inertial and viscous forces [43]:

$$Re = \frac{v_m D_h}{\mu_k} \tag{3}$$

where v_m is the mean fluid velocity [m s^{-1}] and μ_k is the kinematic viscosity [m^2 s^{-1}]. The kinematic viscosity μ_k can be calculated ($\mu_k = \mu_d\,\rho^{-1}$) from its dynamic viscosity μ_d [kg m^{-1} s^{-1}] and ρ the density [kg m^{-3}] of the fluid. The Prandtl number Pr represents the ratio of momentum diffusivity to heat diffusion in fluids [43]:

$$Pr = \frac{\mu_k}{\alpha} = \frac{\mu_d c_p}{\lambda} \tag{4}$$

Here, the momentum diffusivity is expressed by μ_k the kinematic viscosity [m^2 s^{-1}]. Further, α is thermal diffusivity of the fluid [m^2 s^{-1}], μ_d its dynamic viscosity [kg m^{-1} s^{-1}], c_p its specific heat capacity [J kg^{-1} K^{-1}] and λ its thermal conductivity [W m^{-1} K^{-1}].

Based on this, it was calculated that at temperatures above 300 °C at the inner surface of the cooling channel with a diameter of 12 mm and the parameters specified in Table 2, the water begins to boil so intensely that a gas film forms. Since such gas films have an insulating effect, this may lead to overheating of the component. Accordingly, the HHF studies should be designed in a way that the temperature on the inner surface of the cooling channel remains below 300 °C.

The thermal stationary module of the Ansys 2020 R1 software was used for the FEM simulations. Thermal simulations of the actively cooled test components during the HHF exposure revealed that, with an incident power density of 14 MW m^{-2} on the top surface of the W double tiles, the maximum temperature on the inside of the cooling channel reaches 291 °C. Therefore, the maximum heat flux of 14 MW m^{-2} was chosen for these HHF studies to prevent excessive boiling and ensure a sufficient safety margin.

Fig. 2 illustrates the temperature distribution in the test component when the two left-hand W double tiles are loaded with 14 MW m^{-2}. Fig. 2A) shows the calculated resulting temperatures of the actively cooled component at steady state loading in color code and isometric view. In this case, the coolant flows from left to right through the component. The white lines in Fig. 2A) indicate the cutting plane for the

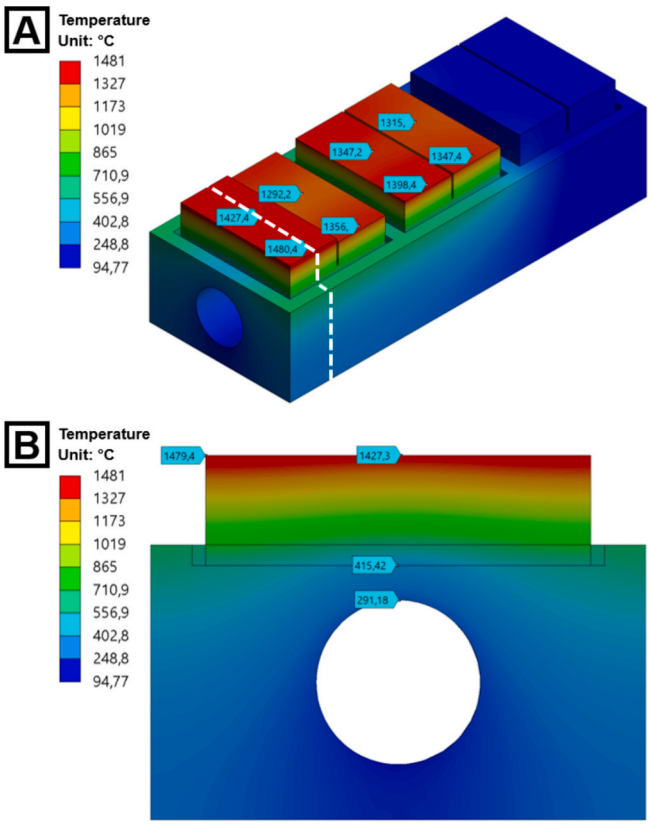

Fig. 2. The temperature distribution simulated by FEM in the test component at steady state 14 MW m^{-2} loading. A) displays the component in the isometric view. Here, only the two W double tiles on the left, which differ in height (8 mm and 7 mm; 7.5 mm and 7.5 mm from left to right), are loaded. The white dashed line in A) indicates the cutting plane for the cross-sectional view depicted in B).

cross section, which is illustrated in Fig. 2B). The resulting surface temperatures on the inner surface of the cooling channel during this thermal loading scenario are illustrated in Fig. 3A) in a cross-sectional view. The maximum temperature of 291 °C mentioned above is reached in the red area. Fig. 3B) shows a cross-sectional view from below of the resulting heat flux on the inner surface of the cooling channel. The thermal energy arriving on the test component at the top of the W double tiles with a heat flux of 14 MW m^{-2} takes the shortest path through the component and is concentrated on the upper surface of the cooling channel to a value of ~22 MW m^{-2} as visible in Fig. 3B). Thus, the critical heat flux on the inner surface of the cooling channel beyond which the component risks overheating is just over 22 MW m^{-2}.

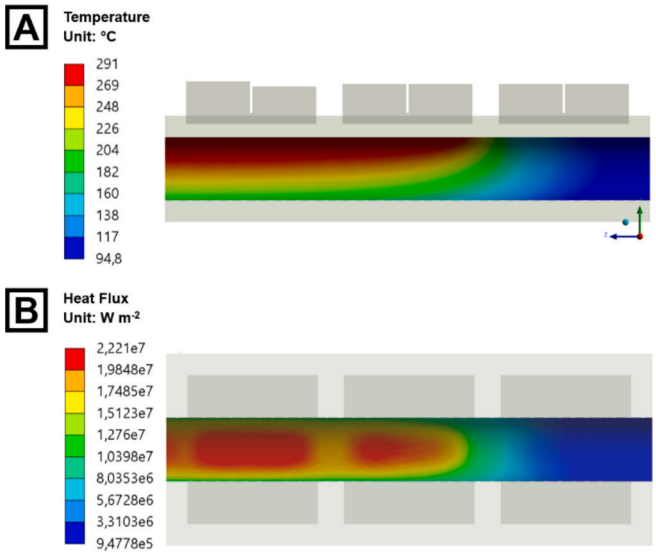

Fig. 3. The temperature distribution A) and the heat flux B) on the surface of the cooling channel at steady state loading of the left two W double tiles of 14 MW m^{-2} (same scenario as in Fig. 2). A) shows the cross section of the component cut parallel to the cooling channel and B) the component as seen from below, also cut parallel to the cooling channel.

The heat dissipation capability of the test components is slightly lower than that of monoblock components. This is partly due to the absence of swirl tapes in the test components, which were not used cause of simplification. Swirl tapes cause increased fluid turbulence, which leads to higher Reynolds numbers *Re* and thus increases the cooling capacity of the component through convective heat transfer h_{cv} (see equations (1) to (3) [44]. In addition, slightly higher flow rates, cooling water pressures, and water temperatures are typically used in monoblock components. This difference in cooling performance means that, at 14 MW m^{-2} loading, the resulting surface temperatures on the loaded surface (see Fig. 2, left half of the left W double tile with 8 mm height) at the test component are as high as those of monoblock chains at 15 MW m^{-2} loading (see Table 1). And 9 MW m^{-2} loading on the test components result in temperatures occurring during 10 MW m^{-2} loading on monoblock chains. In the following, the W double tiles at which surface temperatures corresponding to those reached on real monoblock chains in steady state during 10 and 15 MW m^{-2} loading are referred to as such.

2.2. Manufacturing and LMD-w coating of the test components

For the high heat flux tests, three test components like the one shown in Fig. 1 B) were manufactured. Each of these test components features three W double tiles (except for component 3, where the central one is separated). A double forged pure W (DW) blank from the manufacturer Plansee was used as the base material to manufacture these tiles [32,45,46]. The double tiles were cut from the W blank using electrical discharge machining (EDM). To achieve the T-orientation of the grains, which is desired for plasma-facing material, the W tiles were cut from the blank in a defined alignment. T–orientation means that the grains are elongated transversal to the loaded surface. This grain elongation transversal to the stressed surface reduces the likelihood of individual grains breaking out of the W matrix [47]. Since impurities of high Z materials like W cause the plasma to cool down significantly, thereby impairing the performance of the fusion reactor, these impurities should be kept to a minimum [13].

The W tiles were coated with W using the LMD-w process, which is schematically illustrated in Fig. 4A). This coating is intended to simulate the regeneration of W armor of PFCs whose thickness was reduced by erosion. Here, the aim is to test the resilience of the regenerated armor under fusion–relevant thermal conditions. Fig. 4B) depicts one of the double tiles shortly before the LMD-w coating, and C) depicts one LMD-w coated W double tile. For the coating procedure, the process parameters listed in Table 3 were applied, which demonstrated the most favorable results when utilizing this specific LMD-w setup. One respectively two W layers of about 0.65 mm height were applied onto the W double tiles. Pure W wire from Osram Licht AG with a diameter of 1 mm was used for the deposition. The laser source is a Laserline GmbH (model LDF 5000–40) diode laser that generates a continuous wave laser beam with a power of up to 5 kW. The diodes emit light at wavelengths of 910, 940, 980 and 1030 nm. The light is guided from the laser source to the optical system via glass fibers. The optical system is water–cooled and directs the light onto the substrate to a 2 mm diameter focal point with a focal length of 139 mm. A system from Arbicor Binzel was used for the W wire guidance. Here, the wire is fed from a 45° angle into the melt pool. The machine control in x-, y- and z–direction, the control of the laser and the inert gas flow is managed by a modified 3-axis computerized numerical controlled (CNC) Rexroth control unit. During the process, the

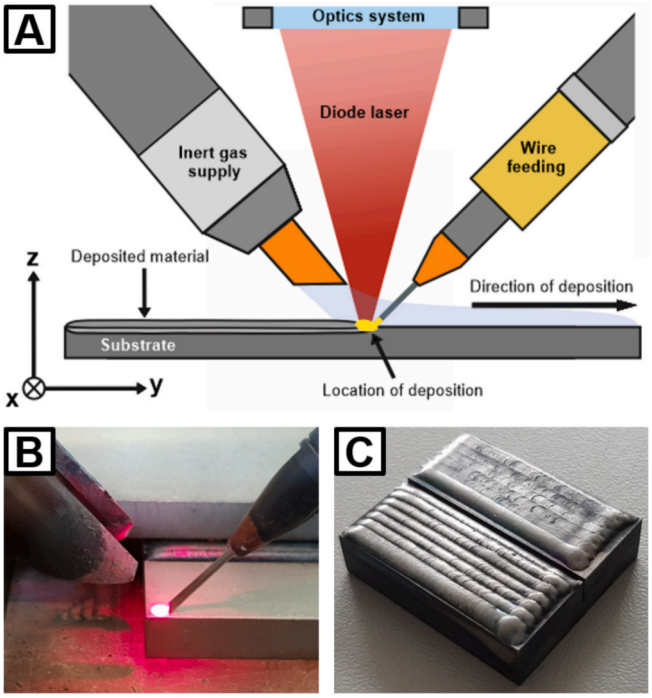

Fig. 4. In A), a schematic representation of the LMD-w process is illustrated (reproduced from [29]). B) is an image taken shortly before coating a W double tile. Here, the pilot laser spot, which is used for positioning, and parts of the LMD-w setup are visible. C) depicts one of the coated W double tiles. On the two upper surfaces of this double tile, each measuring 28 × 12 mm^2, W was deposited by LMD-w. The surface on the lower left was coated with one regular layer, and the one on the upper right was coated with one layer smoothed by laser remelting.

Table 3
Process parameters used to generate the LMD-w W coatings.

Process parameter	Symbol	Value	Unit
Energy density	E_n	477	J mm^{-2}
Projected area energy density	E_a	375	J mm^{-2}
Line energy input	E_t	750	J mm
Laser power	P	5	kW
Beam diameter	d_s	2	mm
Deposition velocity	v_s	400	mm min^{-1}
Wire fed velocity	v_w	500	mm min^{-1}
Hatch spacing	h_d	1.51	mm

heated material is protected from oxidation by inert gas in the form of argon with 99.996 % purity, which is directed onto the material via an actively cooled nozzle with a gas flow rate of 15 l min^{-1}. During the LMD-w process, welding beads are deposited on the substrate in a dragging process (i.e., front feeding process), as shown schematically in Fig. 4A). During the LMD-w process, the W tile heats up. To ensure constant substrate temperature and thus reproducible process conditions throughout the entire process, the W tiles are thermally stabilized by the underlying copper cooling plate. The W tiles are pressed against the copper plate by means of a clamping system. This copper plate features cooling channels through which 19 °C water flows. This also prevents undesired oxidation of the W tiles.

A common way of comparing the energy input in direct energy deposition (DED) processes and metal additive manufacturing (AM) in general is to specify the energy density [22]. A widely used and reasonable approximation is the projected area energy density E_a [J mm^{-2}] [48,49]:

$$E_a = \frac{P}{v_s d_s}\left[\mathrm{J\,mm^{-2}}\right] \tag{5}$$

where P [W] is the laser power, d_s [mm] the diameter of the laser focal spot and v_s [mm s^{-1}] the scanning velocity. For increased comparability across studies with various laser spot shapes, the energy density E_n [J mm^{-2}] is calculated as follows [50]:

$$E_n = \frac{P}{v_s \frac{A_s}{d_\parallel}}\left[\mathrm{J\,mm^{-2}}\right] \tag{6}$$

where A_s [mm^2] is the surface area of the laser spot and $d_\parallel$ [mm] is the spot diameter parallel to the deposition direction. However, the simple line energy input E_t [J mm] is also frequently used as a measure of energy input [22]:

$$E_t = \frac{P}{v_s}\left[\mathrm{J\,mm}\right] \tag{7}$$

To ensure better comparability across studies, the values for E_a, E_n and E_t are provided here. The parameters specified in Table 3, which were considered to be the most promising according to earlier parameter studies, were used to deposit the LMD-w W coatings [29].

Additional laser remelting was used to further smoothen several of the coated surfaces. In this remelting process, the surface is melted again via laser to achieve smoothing of the coating surfaces. For this smoothing process, the same process parameters were used as for the LMD-w process, which are specified in Table 3, but the wire feeding was deactivated. For this study, the laser remelting was performed with the same scanning direction as used for deposition, as single remelting in the same direction had a larger effect than perpendicular to the deposition direction. For remelting parallel to the deposition direction, the laser spot is centered and moves along the elevated regions of the coating (moves along the welding beads) causing them to melt and the material to accumulate in the deeper regions, resulting in a smoother surface. This effect can also be observed for perpendicular remelting, but not as strongly because the laser is not centered or moves especially along these elevated regions. The W_t value can be used to measure surface waviness. W_t is the difference between the highest and lowest points of a low–pass filtered profile over a defined length. To determine the profile, a laser profilometer from OPM GmbH equipped with a KF3 confocal sensor was used. The surface areas of various coatings, as well as coated and subsequently smoothed layers, were measured. In an earlier study, the waviness W_t of an LMD-w coating was reduced from ~160 µm to ~100 µm by remelting perpendicular to the deposition direction [29]. Remelting parallel to the deposition direction has proven to be even more effective in smoothing the surface, reducing surface waviness W_t to a value of ~70 µm.

The W double tiles to be coated are initially 7 mm high instead of 8 mm to simulate eroded W armor. Coating these tiles with one LMD-w layer increases their initial height of 7 mm to ~7.65 mm. The ones coated with two stacked layers measure ~8.2 mm in height after LMD-w coating. After laser remelting, the maximum height of these tiles is reduced by ~50 µm. Through controlled melting of the material during this laser remelting post process, material from elevated areas flows into depressions, thus smoothing the surface and slightly reducing the maximum height.

Three cooling structures were manufactured from pure copper blanks by computerized numerical control (CNC) milling. The geometry of the cooling structures is visible in Fig. 1B). They each feature one cooling channel with a diameter of 12 mm through which the coolant will flow during the HHF experiments. Three 26.5 × 29.5 cm pockets with depths of 1.5 mm are milled into the top of the cooling structure, into which the brazing foil and the W double tiles are placed for joining. The W tiles are brazed to the copper cooling structures, using 100 µm thick AgCu28Ge2Co0.3 brazing foil. This brazing solder is only used for

the purpose of mock-up fabrication and not suited for the use in real divertor components, due to the long term neutron activation of silver. This Ag–based solder is frequently used for joining 12 × 12 × 5 mm^3 W material samples with copper cooling structures for fusion–relevant HHF material qualification experiments and has proven to be reliable [32]. It was therefore utilized in the HHF experiments of this study. This alloy has a melting temperature of 780 °C. Brazing was carried out in a vacuum furnace at a peak temperature of 850 °C over a period of 15 min. Heating and cooling took place at controlled rates of 13 K min^{-1}.

For the HHF experiments, the prepared three test components were connected to the cooling system of the JUDITH 2 electron beam facility using clamping elements. Fig. 5 depicts the three components shortly before the HHF tests. Which tiles were exposed to which loading scenario is marked in Fig. 5. Of the six 28 × 12 mm^2 W surfaces of component 1, three were coated with one normal layer and three with one normal layer that was subsequently smoothed by laser remelting. Component 2 was treated in the same way, but with two stacked layers. Component 3 features four surfaces (red framed), onto which one layer was deposited, and two uncoated surfaces (black framed), which serve as reference. The upper half of the uncoated reference double tile visible in Fig. 5 is 8 mm high, and the lower half is 7 mm high. The two center W tiles on component 3 were not connected as a double tile and shifted slightly during the brazing process. This demonstrates why W double tiles were selected to maintain the mentioned 0.5 mm gap. Fig. 5 reveals that the coated surfaces on component 2, with two stacked layers, exhibit more defects such as porosity and surface irregularities than the single layer coatings of component 1. These defects and irregularities are the result of minor process instabilities, which are addressed in the discussion section.

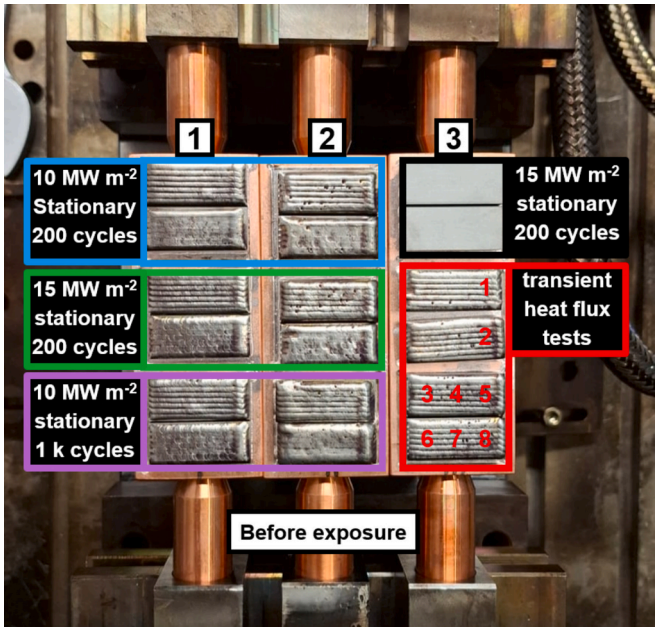

Fig. 5. Components 1 to 3, here already connected to the cooling unit of the electron beam facility JUDITH 2, shortly before exposure to cyclic steady state (blue, green, purple and black framed) or combined steady state and transient heat fluxes (red framed). The W double tiles, which were coated with W by LMD-w with the exception of the uncoated reference (black framed). The red numbers indicate the positions listed in Table 4 where certain combined steady state and transient HHF scenarios were performed, to simulate the thermal impact of ELMs on the LMD-w coatings. (For interpretation of the references to color in this figure legend, the reader is referred to the web version of this article.)

2.3. Steady state thermal load exposure

In the steady state high heat flux experiments, the test components were loaded according to the plan in Fig. 5 (framed in blue, green, purple and black). To ensure even distribution of the heat load across the defined area, the electron beam is rapidly moved in a grid pattern. This grid pattern is achieved by directing the beam to specific points in a two–dimensional coordinate system. The electron beam has a Gaussian profile with a diameter of around 5 mm (at full width half maximum). Magnetic lenses enable the electron beam flow to be focused and moved in a defined manner by changing the magnetic fields. Since the electron beam works in continuous operation, it needs to be positioned on specially designed beam dumps whenever it is not required. These beam dumps are copper structures that are actively cooled by purified water. The cooling system achieves the cooling performance of 150 kW for the beam dumps. The vacuum chamber is also actively cooled and can dissipate 80 kW. The cooling circuit for test components reaches a maximum cooling performance of 150 kW [32,33]. The absorbed heat flux on the test components is determined by water calorimetry (temperature measurements of the cooling water at the inlet and outlet).

During the HHF experiments, the surface temperature of the W double tiles gets monitored using two–color pyrometry and high–speed pyrometry. The two–color pyrometer is used to calibrate the high–speed pyrometer (which is particularly relevant for transient exposure tests in the next subsection). Fig. 6 is the plot of surface temperature measurements on surfaces with two stacked normal layers during the cyclic 10 and 15 MW m^{-2} exposure experiments. The tiles with two stacked layers are ~8.2 mm high. Surface temperatures of 1000 °C and 1500 °C were measured during the loading phases (see Fig. 6). Thus, the surface temperatures specified in Table 1 are reached during the exposure experiments, which are equivalent to those on monoblock components at 10 and 15 MW m^{-2} loading. According to the pyrometer measurements plotted in Fig. 6, the temperatures during the no exposure phases were measured to be ~400 °C, which is just the lower measurement limit of the respective single–color pyrometer. In reality, the temperatures drop to the temperature of the coolant (70 °C) during the no exposure phases. Each test cycle consists of 20 s of loading and 20 s of no exposure. During both the loading and no exposure phase, the steady state is achieved. Each of these 40-second cycles simulates one plasma discharge of a large–scale fusion reactor. Even though the plasma discharges of future

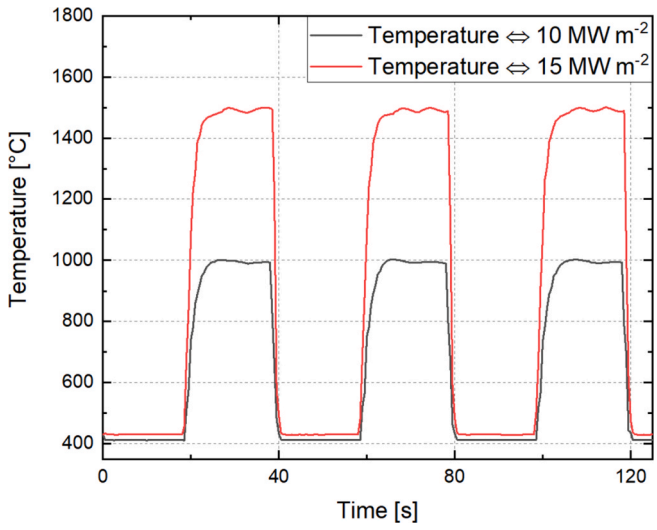

Fig. 6. The temperatures measured by the high–speed single–color pyrometer during cyclic steady state exposure on surfaces of component 2, each coated with two stacked LMD-w layers (normal layers). Each loading cycle simulates the thermal impact of one plasma discharge of a large scale fusion reactor on its PFCs.

fusion power plants will last much longer, 20 s is sufficient for these tests, since the number of temperature changes (exposure cycles) is the main factor determining the lifetime of PFCs and especially their joints. In Fig. 5, the four surfaces which are subjected to 200 cycles at 10 MW m^{-2} are framed in blue. The tiles framed in green are exposed to 200 cycles at 15 MW m^{-2}. The uncoated reference tiles framed in black are also exposed to 200 cycles at 15 MW m^{-2}. And the ones framed in purple are exposed to 1000 cycles at 10 MW m^{-2}.

Fig. 7 illustrates infrared (IR) camera images of 1 layer and 1 smoothed layer coatings during loading cycles 1 and 1000 of the 10 MW m^{-2} thermal loading experiments. For all coatings, the measured average surface temperatures across all 10 MW m^{-2} loading cycles remained constant at around 1000 °C (both for 200 and 1000 cycles). In Fig. 7, a crack parallel to the cooling channel is indicated by black arrows. Fig. 8A) is the IR camera image of the uncoated reference W double tile during the first loading cycle. B) shows the same double tile during loading at cycle 200. Since temperature measurements are an essential part of the thermal loading experiments, accuracy is of paramount importance. The IR camera and the high–speed single–color pyrometer were calibrated using a two-color pyrometer which was directed onto the same position. Two-color pyrometry enables reliable, much less emissivity dependent optical temperature measurements. However, this emissivity independence is only valid if it is independent of the wavelength (gray body assumption). Furthermore, the temperatures measured by two–color pyrometry at the start of the HHF experiments corresponded to those calculated using FEM simulations. Hence, the emission coefficient for the IR camera and the high–speed single–-color pyrometer were set to corresponding values based on the two–-color pyrometer measurements. Since the emission coefficient can change due to surface modifications and temperature changes, it had to be recalibrated frequently during the experiments. In Fig. 8, the upper half of the double tile measures higher surface temperatures than the lower half. This can be explained by the fact that the upper half of the W double tile measures 8 mm in height and the lower half 7 mm. The surface temperature of this uncoated reference double tile increased with increasing cycle count. This behavior is evident in the IR camera images (compare Fig. 8A) and B)). The relative changes in average surface temperatures from loading cycle 1 to cycle 200 were analyzed for all areas subjected to the steady state 15 MW m^{-2} HHF scenario. These relative changes in average surface temperatures of the various coated and uncoated W surfaces are visualized for comparison in Fig. 9. The measured average surface temperatures at the last loading cycles either remain unchanged (see 1 layer) or increase by up to 36 % of that at the first cycle. This temperature increase occurred cumulatively as the count of loading cycles rose. In addition, the IR camera image in Fig. 8B) displays a crack running centrally through both halves and parallel to the cooling channel. Also, the left side of the double tile at cycle 200 in Fig. 8B) shows an elevated temperature. This crack developed during cyclic HHF tests.

Fig. 10 shows the IR camera image of two double tiles covered with different coatings during the 200th loading cycle of the 15 MW m^{-2} HHF experiments. These are the two W double tiles framed in green in Fig. 5. On the left double tile, one layer was applied to the upper 28 × 12 mm^2 surface and one layer to the lower surface, which was subsequently smoothed by laser remelting. On the right double tile visible in Fig. 10, two stacked layers were applied to the upper surface and two stacked layers to the lower surface, which was also smoothed by laser remelting.

2.4. Combined steady state and transient thermal load exposure

In large-scale fusion reactors, type–1 ELMs can impose thermal loads in the GW m^{-2} range onto the surface of the PFM [51,52]. This means significant stress for the PFM and poses a major challenge for its durability [10]. Therefore, as part of the HHF experiments the influence of giant ELMs on LMD-w coated PFCs was simulated in various loading scenarios with combined steady state and transient thermal loads.

In accordance with the plan of Table 4, the four single layer coatings framed in red in Fig. 5 were loaded. The red numbers in Fig. 5 indicate the positions referred to in Table 4. The base temperature T_{base} defined in Table 4 is created on the W surfaces in the test facility by directing the electron beam at high velocities in a grid pattern across the coated surfaces. This way, steady state thermal loads are simulated. Along with this steady state loading, transient thermal loads (or thermal shocks) are added. This is achieved using the circular beam loading method [32]. In this method, the electron beam travels along eight points across circle. This circle is traversed 12 times during one thermal shock, whereby each orbit takes 40 µs. This results in thermal energy being deposited in a circular area within the total pulse duration of 0.48 ms. The resulting rise in surface temperature ΔT [K] due to transient thermal loads striking the surface of a semi–infinite body can be approximated as follows [4,53]:

$$\Delta T = 2L\sqrt{\frac{\Delta t}{\pi\lambda\rho c}}[\mathrm{K}] \tag{8}$$

Here L [W m^{-2}] stands for the power density and Δt [s] for the pulse duration. In the context discussed here, λ is the thermal conductivity of W ($\lambda \approx 120$ W m^{-1} K^{-1} at 1000 K), ρ its density (19.12 g cm^{-3} at 1000 K)

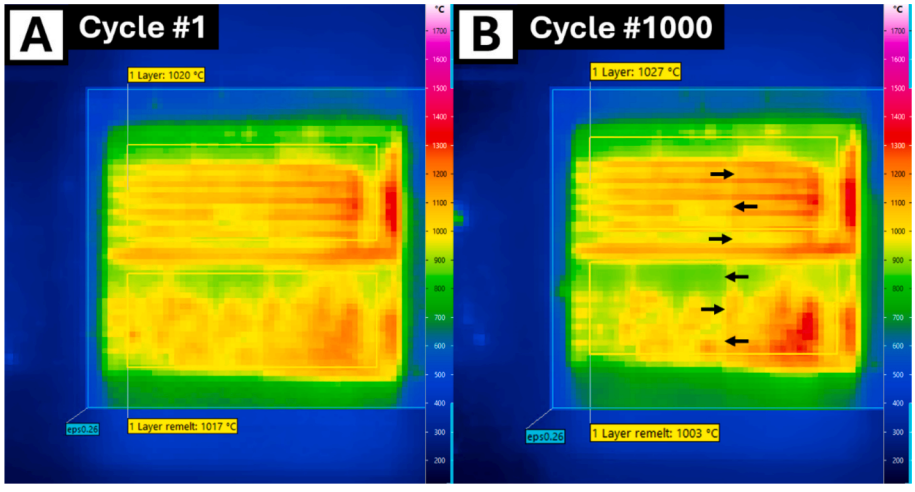

Fig. 7. Exemplary for all coatings loaded at 10 MW m^{-2}, shown at the upper side is 1 layer and at the lower side 1 layer smoothed, at loading cycle 1 in A) and 1000 in B). The black arrows in B) mark the position of a crack.

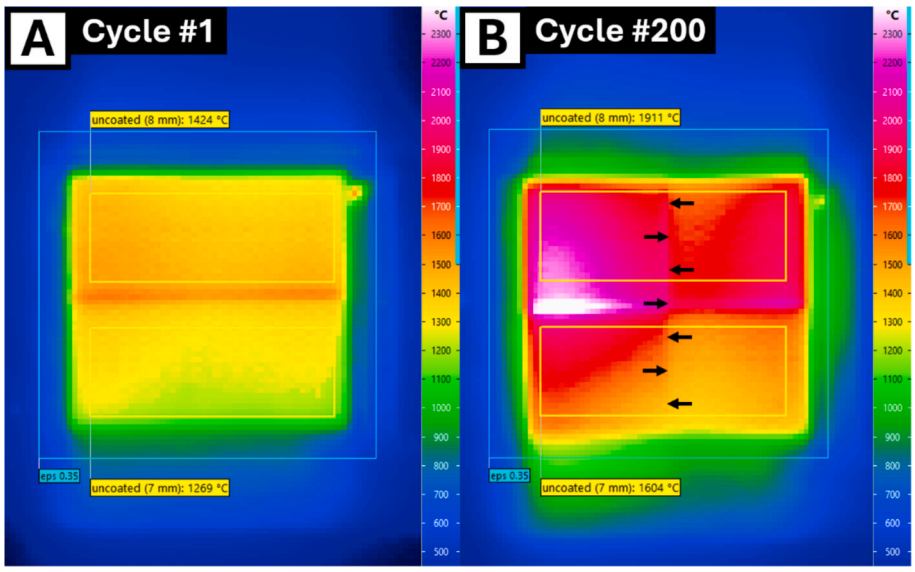

Fig. 8. Infrared camera images of the uncoated reference W double tile during cyclic exposure to steady state heat fluxes of 15 MW m^{-2}. The double tile is displayed in A) during the loading phase of the first cycle and in B) during the 200th cycle. The black arrows in B) mark the position of a crack.

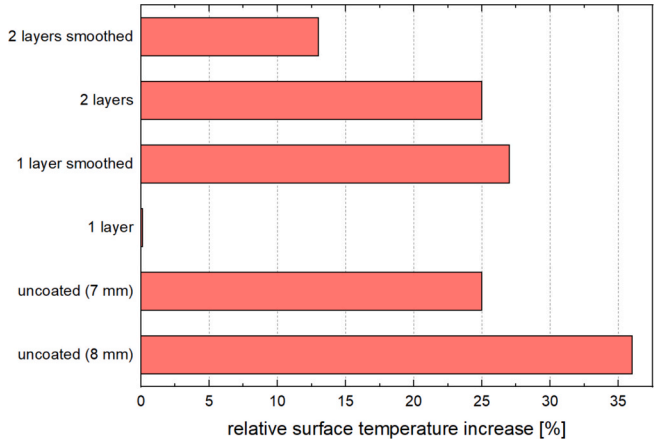

Fig. 9. The relative increase in the measured temperatures of various coated and uncoated W surfaces during the HHF experiments is visualized here. This relative temperature increase refers to the rise in average measured surface temperatures between the 1st and 200th cycle of the 15 MW m^{-2} steady state HHF experiments.

and c its specific heat capacity (150 J kg^{-1} K^{-1} at 1000 K) [10,12]. The power density L and pulse duration Δt can be used to calculate the so–called heat flux factor F_{HF}, which serves as a metric for the temperature increase ΔT from the base temperature T_{base}:

$$\Delta F_{\mathrm{HF}} = L\sqrt{\Delta t}\left[\mathrm{MW\,s^{0.5}\ m^{-2}}\right] \tag{9}$$

As specified in Table 4, various loading scenarios with $F_{HF} = 3$, 6 and 12 MW $s^{0.5}$ m^{-2} were conducted at base temperatures of 200 and 700 °C with 10^3 to 10^5 pulses. The locations are given in Fig. 5, where eight positions are marked with red numbers on the four red framed single layer coatings. The areas at these positions are exposed to combined steady state and transient thermal loads according to the parameters specified in Table 4, to demonstrate and investigate the influence of ELMs on LMD-w coated PFCs.

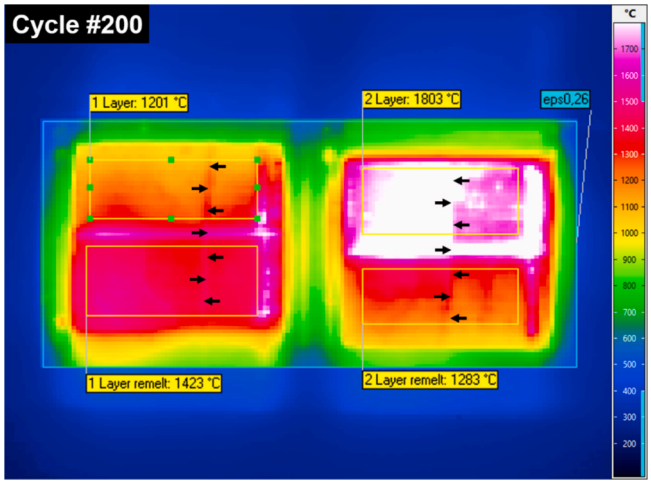

Fig. 10. Displayed is an IR thermography image of two W double tiles (framed in green in Fig. 5) with different coatings during the 200th loading cycle at steady state 15 MW m^{-2} HHF exposure. The black arrows mark the position of cracks.

3. Results

3.1. Steady state thermal load exposure

Fig. 11 depicts the three test components subsequent to the HHF experiments. The W double tiles are framed in color according to the respective loading scenario. Noticeable are cracks on the cyclic steady state loaded surfaces. These cracks run centrally parallel to the cooling channel and extend through both halves of the respective double tiles. These cracks were analyzed in cross–sectional micrographs. Furthermore, the comparison of the surface conditions visible in Figs. 5 and 11 reveals surface modifications. These surface modifications were quantified by laser profilometry measurements before and after the respective HHF exposure scenarios.

Already during the HHF experiments, one crack was visible on the IR imaging of the uncoated reference double tile at 200 cycles of 15 MW m^{-2} loading (see Fig. 8B)). This crack is also visible optically in Fig. 11 (black framed double tile). Cross–sectional micrographs were prepared

Table 4
Loading parameters for the combined steady state and transient thermal loading scenarios at the locations given in Fig. 5.

Position #	Quantity of transient pulses	Pulse length Δt [ms]	Heat flux factor F_{HF} [MW $s^{0.5}$ m^{-2}]	Absorbed power density L [GW m^{-2}]	Base temperature T_{base} [°C]	Peak temperature T_{max} [°C]
1	10^5	0.48	3	~0.13	~700	~900
2	10^5	0.48	6	~0.27	~700	~1050
3	10^3	0.48	12	~0.55	~700	~1450
4	10^4	0.48	12	~0.55	~700	~1450
5	10^5	0.48	12	~0.55	~700	~1450
6	10^5	0.48	3	~0.13	~200	~400
7	10^5	0.48	6	~0.27	~200	~550
8	10^5	0.48	12	~0.55	~200	~950

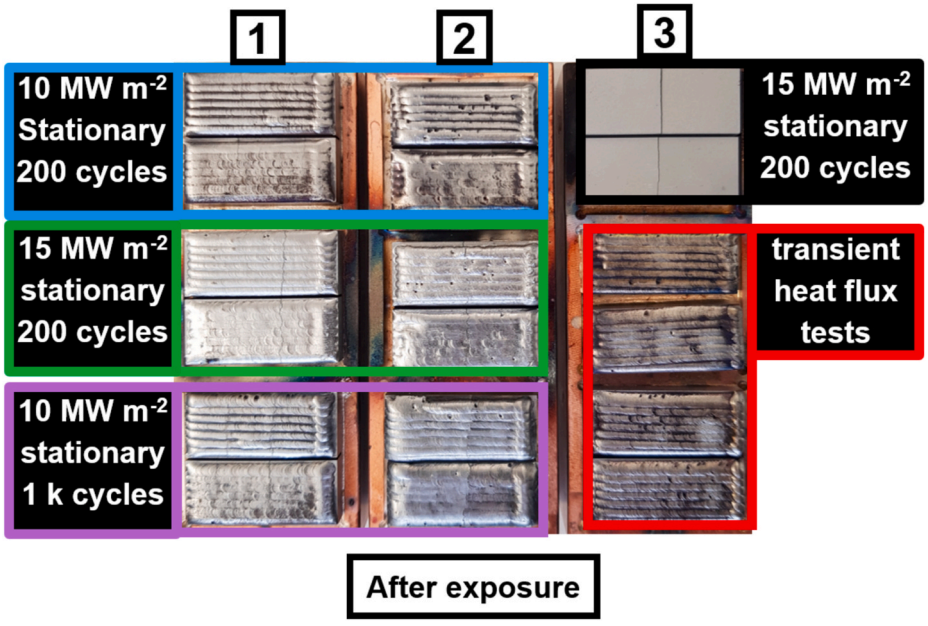

Fig. 11. Condition of the test components after HHF exposure. It is indicated in color which areas were subjected to which thermal loads. The double tiles that were exposed to cyclically occurring steady state heat fluxes partially show cracks that run parallel to the cooling channel (green, purple, black). The blue framed ones do not show any obvious visible changes. The surfaces framed in red, which were subjected to the combined steady state and transient thermal loads according to Fig. 5 and Table 4, partially display circular surface changes corresponding to the areas exposed to transient loads.

with the cutting plane perpendicular to the cooling channel. Fig. 12A) depicts the cross-section of the 8 mm high uncoated reference W double tile. The crack in this tile runs perpendicular to the loaded surface vertically downwards to the copper heat sink, where it ends. The crack developed relatively early during the cyclic HHF tests. At around 20 cycles, the crack was vaguely visible for the first time on the IR imaging.

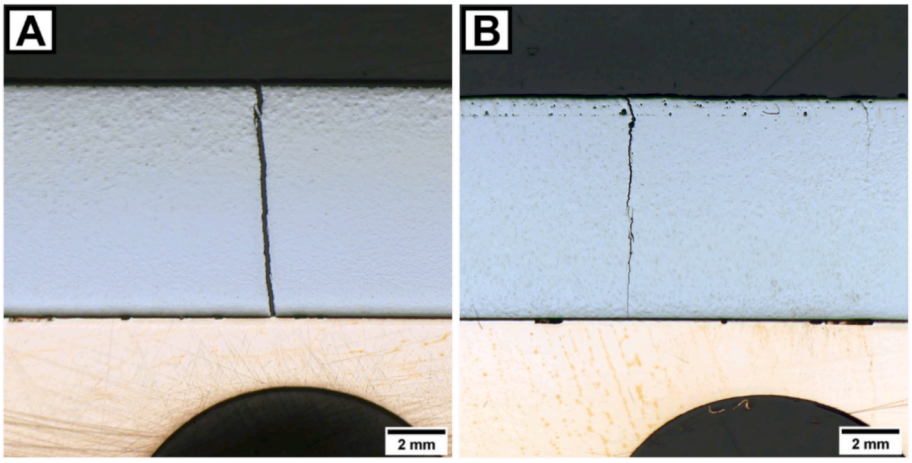

Fig. 12. The components depicted here were exposed to 200 cycles of 15 MW m^{-2}. Both the uncoated W double tile A) as well as the single layer coated one B) exhibit a macro crack running parallel to the cooling channel and transversal to the loaded surface.

With the increasing number of loading cycles, the crack grew.

After exposure to 200 cycles of 15 MW m^{-2}, the coated double tiles framed in green in Fig. 11 show similar large cracks as the uncoated reference. During the HHF experiments these cracks were also vaguely visible on the IR images. They grew in size with an increasing cycle count. Before the HHF experiments, no cracks were obviously visible on the LMD-w coated W surfaces (see Fig. 5). However, upon closer inspection, it became apparent that cracks had already formed during the coating process. Fig. 12B) is the cross-section of a smoothed single layer coated W tile, which also has a crack running vertically downwards transversely to the loaded surface and ending at the copper heat sink. However, this crack is not as wide as the one in the uncoated tile (compare Fig. 12A) and B)). Further, in Fig. 12B), on the right side, another crack that runs ~2 mm deep is visible. It was discovered in cross sections of unloaded coatings that cracks of this type and pores can occur due to deposition of W by LMD-w [29,30]. These kinds of defects are also present in the cross sectional micrographs of Fig. 13. Here, the cutting plane is parallel to the cooling channel. Fig. 13A) displays a single layer, B) a smoothed single layer, C) two stacked layers and D) two stacked smoothed layers. Here, the deposited material lies above the dashed black line, and the substrate material lies below this line. Fig. 13 reveals the seamless joint between the deposited material and the substrate. Furthermore, the connection between the stacked layers in Fig. 13C) and D) is also seamless. The double tiles framed in blue in Fig. 11 were loaded with 200 cycles of 10 MW m^{-2}. On closer inspection they also show cracks parallel to the cooling channel. These cracks have already formed during the LMD-w process and grew slightly due to the HHF exposure. These cracks are not as pronounced as those on the green framed double tiles. The double tiles framed in purple, which were loaded with 1000 cycles of 10 MW m^{-2}, show the same type of cracks. However, due to the higher number of loading cycles, the cracks are more pronounced on the purple framed double tiles.

Fig. 14 shows cross-sectional SEM images of the brazed W/Cu joints of the test components after the HHF tests. Fig. 14A) displays the nearly flawless joint between a W double tile and the copper cooling structure. Here, the light colored upper section is W, the dark lower section is copper, and the layer in the middle is the used silver–based brazing alloy. During the brazing process, pores formed in the brazing solder at the joint, as can be seen in Fig. 14B). Most of the brazed joints look like those in Fig. 14A), with occasional pores as visible in Fig. 14B). Furthermore, partial delamination between W and the brazing material was observed at certain joints. Such a delamination defect is visible in Fig. 14C). It depicts partial delamination that occurred at the edge of the uncoated double tile (black framed in Fig. 11). Unfortunately, the condition of the W/Cu joints of the tested components prior to HHF exposure is unclear, as destructive analysis in the form of cross-sectional micrographs is required for examination. However, if these delamination defects were already present in the components after brazing, they should have been already visible on the IR images in the form of elevated temperatures in certain areas during the first steady state thermal loading cycles. Since this was not the case, it is more likely that these delamination defects at the W/Cu joint only formed during the HHF experiments.

The changes in the surface structure resulting from the HHF exposure were measured using laser profilometry before and after the thermal loading scenarios. Surface roughness was specified in the form of the standard value sR_a (arithmetic average roughness) and the sR_q (root mean square roughness) value [54]. The s before R_a and R_q indicate that these values are measured for a surface area and not just an individual profile line. sR_q was selected because it is more sensitive to individual measuring peaks caused by defects such as cracks. The differences in roughness ΔsR_a and ΔsR_q before and after exposure are listed in Table 5. The measured initial average roughness values before HHF exposure were $sR_a = 1.5(0.6)$ µm and $sR_q = 1.9(0.7)$ µm for the uncoated reference tiles as well as $sR_a = 6.8(0.6)$ µm and $sR_q = 11.7(0.8)$ µm for the coated tiles (here the values in brackets represent the standard deviations). Since cracks were already present in the material of the coated surfaces as a result of LMD-w process, the measured initial sR_q values are higher than the sR_a values. The average increase in surface roughness correlates to the increase of power density and cycle number and amounts to $\Delta sR_a \approx 0.2$ µm for 200 cycles of 10 MW m^{-2}, $\Delta sR_a \approx 0.5$ µm for 1000 cycles of 10 MW m^{-2} and $\Delta sR_a \approx 1$ µm for 200 cycles of 15 MW m^{-2}. For the uncoated reference tiles, the increase in surface roughness of delta $\Delta sR_a \approx 0.17$ µm after 15 MW m^{-2} and 200 cycles is significantly lower than that of the coated tiles. Since cracks have formed or enlarged due to the cyclic HHF exposure, the ΔsR_q values are higher than the ΔsR_a values. Overall, regarding the surface topography, the coatings withstood the cyclic steady state loading scenarios with only slight surface roughening.

3.2. Combined steady state and transient thermal load exposure

The LMD-w coated surfaces subjected to combined steady state and transient heat fluxes after the exposure are framed in red in Fig. 11. In some of the spots loaded according to Fig. 5 and Table 4, circular surface modifications are visible. The circular surface modifications on the red-framed surfaces that are not located at the positions marked in Fig. 5 were developed during configuration of the electron beam facility for the transient loading scenarios. The surface modifications at the red marked positions were quantified by profile measurements before and after the HHF exposures. The differences in surface roughness on the coated surfaces ΔsR_a and ΔsR_q in relation to the respective loads are listed in Table 6. Since cracks have formed in some spots due to the thermal loading and sR_q value reacts more sensitively to measurement peaks caused by cracks, the measured ΔsR_q values are higher than the ΔsR_a values.

The most significant roughening of the surface caused by HHF loading was detected after 10^5 pulses of $F_{HF} = 12$ MW $s^{0.5}$ m^{-2} at 700 °C base temperature. The coated surface subjected to this treatment is shown in Fig. 15B) in isometric and top view. For direct comparison, Fig. 15A) shows the uncoated surface of an ITER grade Plansee (IGP) W

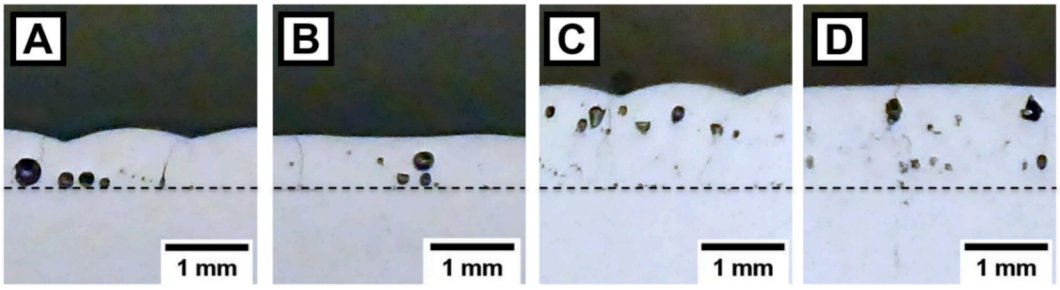

Fig. 13. The cross–sectional micrographs of various coatings cut perpendicular to the direction of deposition after exposure to 200 cycles of steady state 15 MW m^{-2} loading are displayed (green framed double tiles in Fig. 11). The areas above the black dashed line contain the deposited material, while the substrate is located below the line. A) depicts a single layer, B) a smoothed single layer, C) two stacked layers and D) two stacked smoothed layers. The defects apparent in the coatings, like pores and cracks, formed during the LMD-w process. The deposited material exhibits seamless bonding to the substrate and between the stacked layers.

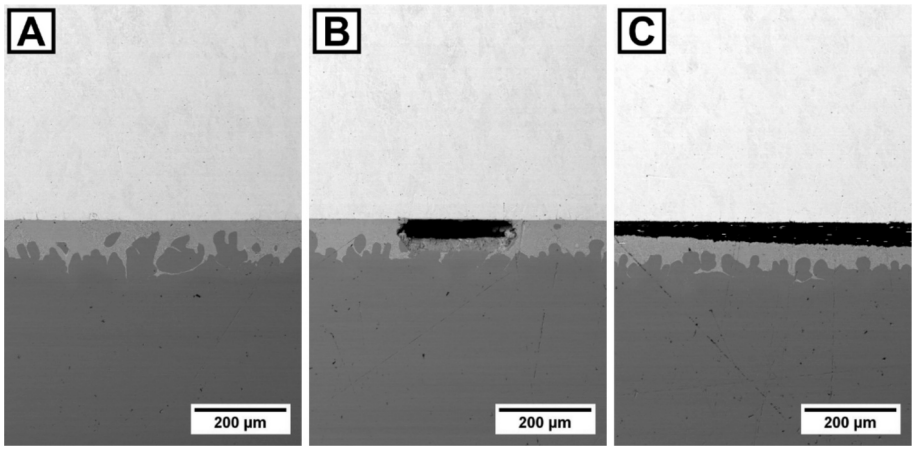

Fig. 14. Three selected SEM images showing the cross section of the brazed joint between W and copper are displayed. The utilized brazing material is a silver alloy (AgCu28Ge2Co0.3). Most of the joints between the W double tiles and the copper cooling structures are intact and appear as visible in Figure A). However, in some cases, pores formed, as visible in Figure B). C) shows the area at the edge of the joint of one double tile that was exposed to 200 cycles of 15 MW m^{-2} steady state loading, which exhibits partial delamination.

Table 5
Specified are the increases in roughness measured by laser profilometry, expressed as ΔsR_a and ΔsR_q, of the uncoated and coated surfaces when subjected to cyclic loading with steady state HHFs. The average measured roughness values prior to the HHF experiments were $sR_a = 1.5(0.6)$ µm and $sR_q = 1.9(0.7)$ µm for the uncoated surfaces as well as $sR_a = 6.8(0.6)$ µm and $sR_q = 11.7(0.8)$ µm for the coated surfaces.

Heat flux [MW m^{-2}]	10		10		15	
Number of cycles	200		1000		200	
Surface roughness parameters [µm]	ΔsR_a	ΔsR_q	ΔsR_a	ΔsR_q	ΔsR_a	ΔsR_q
Uncoated reference	–	–	–	–	0.17	0.25
1 Layer	0.3	0.5	0.97	1.15	0.7	2
1 Layer (smoothed)	0.1	0.27	0.1	0.87	0.9	4.14
2 Layers	0.2	0.9	0.59	1.1	0.9	3.1
2 Layers (smoothed)	0.2	0.34	0.38	0.93	1.75	5.06

Table 6
The increases in roughness on LMD-w layers determined by profilometry measurements before and after exposure to the respective combined steady state and transient thermal loads are listed here. The ΔsR_q values are higher because it reacts more sensitively to cracks than ΔsR_a.

Pulses	Base temperature	$L = 0.13$ GW m^{-2}		$L = 0.27$ GW m^{-2}		$L = 0.55$ GW m^{-2}	
		ΔsR_a	ΔsR_q	ΔsR_a	ΔsR_q	ΔsR_a	ΔsR_q
	[°C]	[µm]	[µm]	[µm]	[µm]	[µm]	[µm]
10^3	700	–	–	–	–	0	0
10^4	700	–	–	–	–	2.35	3.25
10^5	700	0.08	0.15	0.98	1.21	9.92	14.44
10^3	200	0	0.03	0.36	0.48	0.76	1.47

tile from a previous experimental campaign that was subjected to the same HHF exposure scenario [30]. In Fig. 15, the cracks within the uncoated material A) appear slightly deeper and larger than those in W deposited by LMD-w B). The fact that the measured roughness increase of $\Delta sR_q = 23$ µm for the uncoated surface is slightly higher than that of the coated surface of $\Delta sR_q = 14$ µm supports this observation. The ΔsR_a value of the uncoated tile ($\Delta sR_a = 16$ µm) is also slightly higher than that of the coated tile ($\Delta sR_a = 10$ µm). Nevertheless, the surface modifications caused by combined steady state and transient thermal loads for the uncoated and coated tiles are still in a similar range.

4. Discussion

4.1. Coating the components by LMD-w

This experimental campaign showed that areas of 28×12 mm^2 can be coated with W using the LMD-w process with good reproducibility. Further, the coatings did not flake off during the HHF tests and showed good adhesion to the substrate even after exposure to the different loading scenarios. This seamless connection to the substrate enabled good transfer of thermal energy to the underlying substrate material.

However, the cross–sectional images of the coatings prepared after the HHF studies revealed cracks and pores (see Fig. 13). Some of these cracks can be attributed to the high temperature gradients during LMD-w process and were already present in the deposited material before HHF exposure. The formation of these cracks can be prevented by flattening the steep temperature gradients between the melt and the substrate material during the LMD-w process. These temperature gradients cause residual tensions to build up in the material during cooling, which can discharge in the form of these cracks.

In addition, seemingly randomly distributed pores are visible on the cross–section images. These pores can most likely be attributed to process instabilities caused by lateral oscillations of the wire as it is fed into the melt pool during LMD-w as well as suboptimal alignment of the inert gas nozzle. The amplitude of these oscillations can be reduced by lowering the distance between the wire feeding nozzle and the melt pool. When doing so, it is important to ensure that this distance remains large enough to prevent the wire feeding nozzle from melting during the deposition. Further, the inert gas nozzle should also be moved slightly closer to the melt pool to ensure uniform and complete coverage of the melt pool with inert gas. To investigate whether certain defects could be related to the inert gas or ambient gases, further studies of this process could be performed under vacuum. With comparatively low energy input and high viscosity, the process is particularly susceptible to the aforementioned process instabilities caused by inaccurate wire feeding, which can lead to gas inclusions. Since in the process discussed here, the molten W exhibits a comparatively high viscosity, which is recognizable from the surface waviness of the LMD-w layers, the pores may be gas inclusions. On the other hand, at high energy inputs, which lead to deeper melt pools with low viscosity, pores can form during the process due to separation from the vapor capillary in the melt pool (keyhole defects) [55]. To investigate the origin of these pores conclusively, experiments on a facility with higher available laser power would probably be necessary to study the process over a broader range of parameters.

During stacking of layers, surface irregularities of the previously

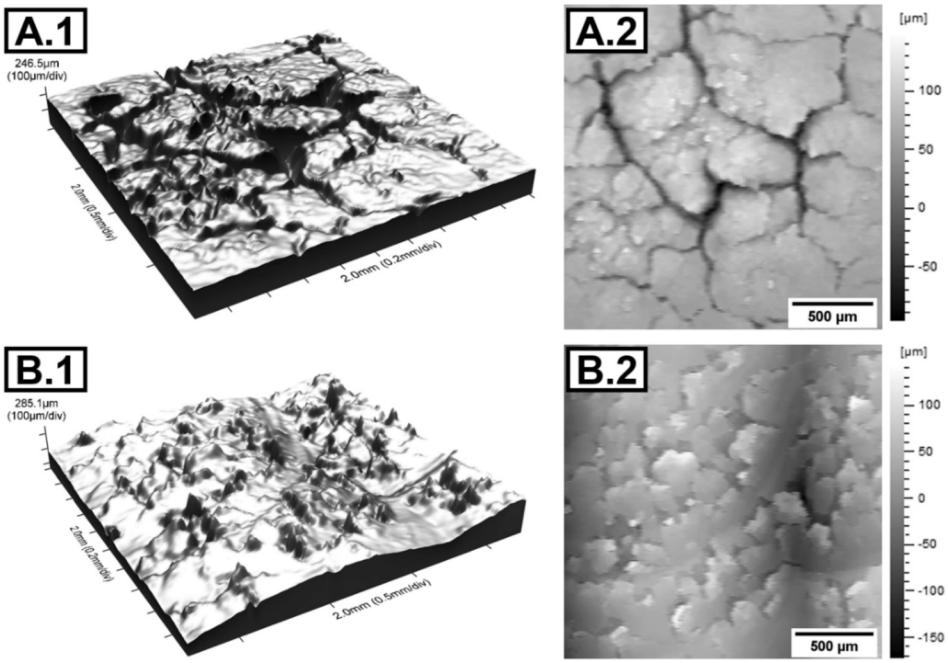

Fig. 15. Laser profilometry measurements of W surfaces that were subjected to combined steady state and transient thermal loads are visualized (10^5 pulses of F_{HF} = 12 MW $s^{0.5}$ m^{-2} at 700 °C base temperature). A) displays an uncoated IGP W surface, which serves as a reference, from previous studies in isometric view A.1) and in top view A.2) [30]. B) shows the surface of a single layer of W applied by LMD-w after the same HHF exposure scenario. B.1) depicts the coated surface in isometric view and B.2) in top view.

deposited layers can also lead to process instability by slightly deflecting the wire. Nevertheless, the connection between stacked layers remains seamless (see Fig. 13) even when multiple layers are stacked [29].

4.2. Steady state thermal load exposure

In the steady state HHF exposure campaign, the resilience of W coatings applied by LMD-w was tested at fusion–relevant thermal loading conditions. The performance of coated W double tiles was compared with that of uncoated references. Each loading cycle in the steady state HHF experiments simulates the thermal stresses exerted on the PFCs inside a fusion reactor by one plasma discharge. In this experimental campaign, all coatings retained their flawless bond to the substrate across all exposure scenarios (see Figs. 11 and 13). This good connection to the substrate enables the coatings to successfully fulfill the main function of PFM, which is to withstand the incoming stresses and conduct energy to the cooling structure. Furthermore, none of the loaded surfaces showed loss of material by spalling. Regarding the resilience to cyclically occurring HHFs, no significant difference between normal, smoothed and stacked W layers applied using LMD-w was observed. In earlier studies, it was already demonstrated that it is possible to stack four LMD-w W layers with flawless interlayer bonding to achieve total layer heights of 2 mm [29]. Compared to alternative deposition methods for W such as plasma spraying or sputtering, the LMD-w process offers the following advantages in addition to those already mentioned (see section 1. Introduction):

- LMD-w W layers seem to withstand HHFs similar to uncoated W due to their seamless bonding to the substrate.
- LMD-w can be performed under normal atmospheric conditions, since it only requires local inert gas shielding.
- LMD-w allows the application of layers of almost any height by stacking them.
- Due to high deposition efficiencies, wire-based processes do not contaminate the reactor interior as powder-based processes would.

In the following it is discussed in detail which layers performed how under which loading scenarios. The mean temperatures measured on the coated surfaces tested at 10 MW m^{-2} remained constant at ~1000 °C across all loading cycles. This applies to both the coatings subjected to 200 cycles (Fig. 11, green frame) and 1000 cycles (Fig. 11, purple frame). In the loading scenario with 1000 cycles, at some point cracks appeared on the IR camera images running parallel to the cooling channel. With the increasing number of cycles, these cracks grew, so that after 1000 cycles they are clearly visible on the purple framed surfaces in Fig. 11. It is unclear whether these cracks originated during the LMD-w process and grew as a result of the cyclic loading, or whether they were newly developed during the HHF exposure. However, it should be noted that due to their position (centrally located on the double tiles) and orientation (parallel to the cooling channel), these cracks are more likely to arise during the HHF experiment than during deposition process. Due to the centrally located cooling channel, the temperature distribution inside the W double tiles is not uniform (see Fig. 2B)). In addition, the temperature shifts of ~900 K between the loading phase and no exposure phase during the cyclic exposure cause changing residual tensions in the material. These tensions are caused by thermal expansion of the material during the loading phase and shrinkage during the no exposure phase. The uneven temperature distribution in combination with the cyclically changing residual tensions could be the origin of these cracks and do in any case cause them to grow. Here, further influencing factors are the dimensions of the test components and the quality of the specific W material.

The resilience of uncoated and coated W double tiles was tested and compared in the 15 MW m^{-2} experiments. Cracks were already visible on the IR camera images after the first few cycles, both on the uncoated and coated surfaces (see Figs. 8 and 10). These are the same type of cracks, that run parallel to the cooling channel and also occurred in the 10 MW m^{-2} 1000 cycle experiments. The fact that cracks with similar appearance also developed on the uncoated reference indicates that the origin of this crack type is not the LMD-w process but the HHF exposure. The aforementioned uneven temperature distribution within the double tiles during loading (see Fig. 2B)) in combination with the alternating

thermally induced expansion and shrinkage of the material is most likely triggering the formation of these cracks. The large temperature shifts of 1400 K between the loading phases and no exposure phases during the 15 MW m^{-2} experiments cause residual tensions within the material. This contributes to the observed growth of these cracks. They are displayed in the cross–sectional micrographs of the uncoated double tile in Fig. 13A) and the single layer coated one in B). This type of crack, running parallel to the cooling channel and transversely to the loaded surface, can also occur in monoblock components. In comparable HHF studies, this defect type occurred in monoblock components after cyclic loading with ~20 MW m^{-2} [37,56–60]. The fact that these cracks occurred in the components tested here even at lower steady state HHFs may be due to the specific W material used for these double tiles. The expectation was that the coatings, rather than the substrate material, would be the weak point in the HHF experiments. Hence, double forged pure W (DW) material was used in the experiments discussed here since it was more readily available than IGP W, which is typically used for monoblocks [10,61]. Both materials are from the manufacturer Plansee and have a grain structure that is elongated transversely to the loaded surface, achieved by forging. DW has pancake–shaped grains and IGP W has needle–shaped grains. Furthermore, the two mentioned W materials have slightly different degrees of purity. These factors can influence the resilience against formation of cracks under fusion–relevant thermal loads [10].

The IR image of Fig. 8B) reveals that the upper left area of the double tile measures higher surface temperatures than its right side. This is most likely caused by the local partial delamination at the brazing joint visible in the cross–section in Fig. 14C). It is not clear whether this partial delamination was already present before the HHF exposure and grew as a result of it or only occurred during the HHF exposure. Partial delamination at the brazing joint can lead to heat accumulation in certain areas of the tiles. To detect such weaknesses in future studies and check the cooling capabilities of the test components prior to the HHF experiments, the IRINA (InfraRed Inspection for Non-destructive Analysis) test facility could be utilized [62]. The IR images of the coated double tiles after 200 cycles (Fig. 10) also show that certain areas of the surface (upper half of the right double tile and lower half of the left double tile) measure increased temperatures. These temperature variations were amplified with increasing number of loading cycles (Fig. 9). To compare the cooling performance of the uncoated and variously coated surfaces at the start and end of the 15 MW m^{-2} experiments, the respective cooling constants were determined (Fig. 16). For the cooling constants,

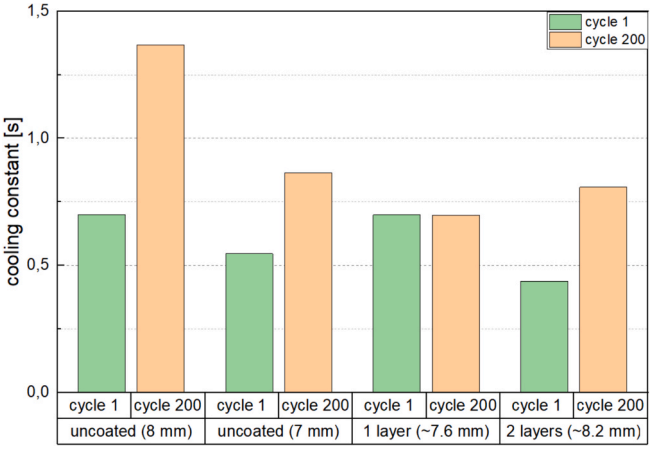

Fig. 16. The cooling constants plotted here represent the ability of the respective coated and uncoated W tiles to cool down after the 15 MW m^{-2} HHF loading. The ability of actively cooled components to rapidly cool down to the coolant temperature has deteriorated for some W tiles during cyclic loading with steady state HHFs. This is evident from the increase of the cooling constants from the 1st to the 200th cycle. Only "1 layer" showed no increase.

the temperature curves during cool down of the component measured on the loaded surfaces by two–color pyrometry were fitted to exponential decay functions. The cooling constant is the duration during which the temperature curve decreases exponentially during cool down. The cooling constants, which are specified in Fig. 16, thus indicate how quickly the respective surfaces were able to cool down after the first and last loading cycle. For nearly all surfaces (except "1 layer" Fig. 16), regardless of being coated or not, the cooling constants increased with increasing cycle count. This indicates that the deterioration in cooling performance is not related to the coatings, but rather to the test components and their deterioration under cyclic HHF exposure. The progressive decline in cooling performance is most likely caused by growing local delamination at the W/Cu brazing joint.

The roughness of the surfaces exposed to cyclic steady state HHFs was measured before and after exposure to evaluate the resilience of the coatings. Increased surface roughness is an indication of accumulating plastic damage and the associated risk of fatigue cracks and erosion due to crack formation. Table 5 lists the corresponding changes in ΔsR_a and ΔsR_q. The measured roughness increased on all surfaces due to the HHF exposure. This was most pronounced on the coated surfaces exposed to 200 cycles of 15 MW m^{-2}. The second highest mean increase in roughness was measured on the coatings exposed to 1000 cycles of 10 MW m^{-2}, and the third highest on the coated surfaces exposed to 200 cycles of 10 MW m^{-2}. The lowest increase in roughness was measured on the uncoated reference surface. However, comparing these increases in roughness with those after the combined steady state and transient HHF scenarios, it is clear that those experienced in the steady state HHF scenarios are all rather low. These low increases in surface roughness in the steady state HHF experiments are therefore another indication of the high resilience of LMD-w W coatings against crumbling or spalling when exposed to fusion–relevant thermal loads. This was expected of pure W with seamless connection to the substrate. Since pure W exposed to high steady state thermal loads usually only shows significant changes in roughness, after long exposure times, due to macroscopic and microscopic deformations caused by creep [63]. The behavior of thermally loaded and thereby predamaged/roughened tungsten surfaces at subsequent plasma exposure has been investigated and discussed in the literature. Subsequent plasma loading can lead to an enlargement of small cracks in the material that were detected in the form of roughness. However, according to the literature the effective sputtering yield of W is not affected by the low roughness values observed here [64,65]. The surface roughness range measured in this study after steady state, as well as combined steady state and transient thermal loading of W armored PFCs has no direct negative effect on the plasma performance of the fusion reactor [65,66].

4.3. Combined steady state and transient thermal load exposure

The resilience of the LMD-w layers to combined steady state and transient thermal loading scenarios was tested on the red framed single layer coated surfaces visible in Fig. 5. In accordance with the plan in Table 4, the positions marked in red in Fig. 5 were exposed to various HHF scenarios. Fig. 11 (red framed area) displays the coated surfaces after being exposed to these loading scenarios. Despite the high thermal stress, no spalling, delamination or crumbling of the coatings is visible.

Further, the coatings were able to dissipate the thermal energy to the substrate without overheating over the entire duration of the tests. In contrast to the 15 MW m^{-2} steady state experiments, no undesirable increase in the mean measured surface temperatures at increasing exposure duration (Figs. 8 and 9) was observed for the coated surfaces in these thermal shock experiments. Even after being subjected to thermal shocks, the deposited material remains good connection to the substrate.

After exposure, surface changes in the form of circular gray spots are visible in Fig. 11 on some of the loaded positions. The change in surface roughness before and after the exposure at the respective positions was quantified by profilometry. Table 6 lists these changes in surface

roughness ΔsR_a and ΔsR_q. The surface modifications are caused by the thermal shocks, which lead to cyclic expansion and contraction of the material. This results in the formation of small cracks through the known damage mechanism [4,10,32,67]. The criterion for crack formation in PFM due to thermal shocks as a result of ELMs, can be described as the relationship between thermal stress and material toughness (Eq. (10)). When the temperature shift ΔT [K] during the thermal shock exceeds a certain value, the ultimate tensile strength σ_{UTS} [Pa] of the material is also exceeded, and cracking occurs [68]:

$$\Delta T > \sigma_{UTS} \frac{1-\nu}{E_M \alpha_{th}} [\mathrm{K}] \tag{10}$$

Here, ν is the dimensionless Poisson's ratio, E_M [Pa] the material–specific Young's modulus, and α_{th} [K^{-1}] its coefficient of thermal expansion. Thus, according to Eq. (10), the strongest crack formation should occur at the loaded positions (see Table 4 and Fig. 5) which experience the highest F_{HF} and thus highest ΔT. Visible surface modifications on the tiles framed in red in Fig. 11 are indeed particularly noticeable at the positions that experienced high F_{HF} and high pulse counts.

The formation of these small cracks can be detected by profilometry. Since cracks are present in the surface after the loading and sR_q is more sensitive to these compared to sR_a, the measured ΔsR_q values in Table 6 are higher than the ΔsR_a values. Fig. 15 visualizes surface topographies measured by profilometry in isometric and top view. A) shows IGP W and B) a single layer LMD-w coating, both after exposure to 10^5 pulses of $F_{HF} = 12$ MW $s^{0.5}$ m^{-2} at 700 °C base temperature. The IGP W surface visible in A) seems to display slightly larger cracks than the LMD-w coated surface. However, the damage pattern on both surfaces still appears comparable overall, which is supported by the similarity of the ΔsR_a and ΔsR_q values. The range of the gray scale in B.2) is broader than that of the IGP surface in A.2) due to the waviness of the coated surface.

The slightly different appearance of the coated and the IGP W surfaces (see Fig. 15) after the HHF exposure may have been influenced by various factors. The microstructure of W materials influences their behavior in response to thermal shocks. Therefore, some relevant characteristics of IGP W and LMD-w W material are compared in Table 7. Here, the term grain structure refers to the direction of grain elongation in relation to the loaded surface. IGP W obtains its grain structure through deformation caused by the forging process. This also strengthens the material. Forged W therefore has an elevated σ_{UTS}, which, according to Eq. (10), leads to a higher damage threshold when exposed to thermal shocks. In comparison, recrystallized and solidified W have lower σ_{UTS} and, consequently, lower damage thresholds with respect to thermal shocks. It should be noted that the deposition of impurities at the grain boundaries during the recrystallization process normally weakens the cohesion of the material. Since LMD-w W is solidified from the liquid phase, it is not as strong as forged IGP W, resembles more the properties of recrystallized W and is therefore expected to start fracturing at lower thermal stresses [10,68]. The elongation of the grains in the LMD-w W transversal to the surface is a result of epitaxial grain growth running vertically upwards during its solidification [29]. In terms of resilience to forces acting parallel to the surface, a longitudinal grain structure would actually be superior to the transversal grain structure. But this transversal grain structure, which is found in both IGP W and LMD-w W, is the preferred grain orientation for PFM. It is because this grain structure makes it difficult for cracks to run longitudinally to the surface, which could lead to material breakout. And, as mentioned, PFM breakout should be avoided because the allowed W impurity level is low to limit radiation cooling of the plasma and preserve reactor operation [13,69,70]. However, it should be noted that after some operating time of the fusion reactor, the PFM recrystallizes in the area close to the surface (up to depths of ~2 mm) regardless of its initial grain structure [20,37,58,71]. This significantly reduces the relevance of the initial grain structure of PFM. Whether the solidified LMD-w tungsten changes its grain structure over time as well, has to be studied in the future.

Table 7
Comparison between characteristics of IGP W and LMD-w W [30].

Characteristics	IGP W	LMD-w W
Manufacturing history	forging	solidification
Grain structure	transversal	transversal
Grain size [μm^2]	550	4000
Grain aspect ratio	3.2	2
Hardness Vickers [HV1]	~440	~370

Overall, the W layers applied by LMD-w withstood the combination of steady state and transient thermal loads similarly to IGP W. And it was shown that transient cracks seem to have no or negligible influence on the macroscopic behaviour of the W double tiles under steady state heat loading.

5. Summary & conclusions

The resilience of LMD-w coated W armored PFCs to the thermal loads expected in large–scale fusion reactors was tested in the electron beam facility JUDITH 2. For this purpose, specially designed actively cooled flat tile test components were used. Various W layers were applied by LMD-w onto W double tiles. This way, the repair of eroded divertor PFCs by LMD-w was simulated.

The following conclusions were obtained regarding LMD-w deposition of W on the plasma–facing surfaces of W–armored PFCs:

- The LMD-w process is capable of coating W surfaces with the typical surface area of the plasma–facing surface of divertor monoblocks of 28 × 12 mm^2.
- The deposition of W via LMD-w is sufficiently precise to maintain the characteristic gap between monoblocks of 0.5 mm. This was demonstrated by the successful coating of the W double tiles as depicted in Fig. 4C).
- W deposited by LMD-w exhibits a seamless connection to the substrate (Fig. 13). Even when several layers are stacked on top of each other, the connections remain flawless (Fig. 13C) and D)).
- Cracks formed in the material during the LMD-w process. These were caused by thermally induced residual tensions resulting from steep temperature gradients between the melt and the colder substrate material. This gradient could be flattened for example by substrate plate heating [72–75].
- Pores are visible in the LMD-w W coatings. These are probably caused by slight process instabilities e.g. lateral oscillations of the wire while entering the melt pool and not powerful enough laser source.

These coatings were then subjected to various thermal loading scenarios, to test their resilience against the thermal impact of multiple fusion reactor plasma discharges. This includes steady state loads of 10 MW m^{-2} with up to 1000 cycles and 200 cycles at 15 MW m^{-2}, as well as ELMs (see Fig. 5). The influence of these fusion–relevant thermal loads on LMD-w coatings was comprehensively observed, analyzed and discussed:

- All of the LMD-w W coatings withstood the steady state thermal loading scenarios without spalling or delamination. No significant variation in the resilience of individual, stacked or smoothed layers was observed with regard to HHF exposure. Thus, unlike alternative deposition processes for W such as plasma spraying or sputtering, LMD-w can be used to apply W layers of several millimeters in thickness that are able to withstand fusion–relevant HHF loading [29].
- Residual tensions occurring during the cyclic thermal loading cause the formation of large cracks running parallel to the cooling channel

and transversely to the thermal loaded surface through the W double tiles (coated and uncoated, see Fig. 12), similar to what was observed in monoblock components [37,56–60].
- The measured changes in surface roughness of the LMD-w coated surfaces (ΔsR_a and ΔsR_q listed in Table 5) resulting from plastic deformation during the cyclic steady state HHF exposure is higher than that of the uncoated reference but remains in a low and acceptable range.

Regarding the influence of combined steady state and transient thermal loads on single layer LMD-w W coatings the following can be concluded:

- The LMD-w layers withstood the combined steady state and transient thermal loads without spalling or delamination (Fig. 11 red framed).
- No increase in the measured average surface temperature was observed, thus, the bond between the coating and the substrate seems unaffected across all transient loading scenarios.
- In direct comparison with IGP W, the W coatings deposited by LMD-w showed a similar damage pattern (see Fig. 15) after the same HHF exposure scenario [4,10,32,67]. Hence, the behavior of LMD-w W at thermal loads, such as those acting on PFCs in the divertor area of large scale fusion reactors during ELMs, is comparable to that of IGP W.

The HHF experiments performed here are only initial investigations to gain an impression of the resilience of LMD-w W coatings towards fusion–relevant thermal loading. Future experiments should be done on IGP W to prevent the substrate from cracking. In addition, improvements on test component design should help assessing the capability of the coating technique and clarify the influence of the brazing. However, since the PFCs in the divertor region of future FPPs will mostly be exposed to steady state heat fluxes of ~10 MW m^{-2}, the obtained findings are already encouraging [9]. The initial surface condition can also influence crack formation, its detectability and growth during HHF exposure. Thus, for a more conclusive and easier comparison of coated and uncoated surfaces, both will be polished to a mirror finish before future tests of this kind. Further improvements of the LMD-w process for the deposition of W should be possible, leading to coatings with fewer defects [29,30]. Since only one version of each type of coating was tested per thermal loading scenario, the reliability of the findings is limited and future repeat studies with larger sample sizes are recommended.

Overall, the LMD-w coatings performed similarly to the uncoated references in both the steady state well as the combined steady state and transient thermal loading experiments. These are promising results with regard to the in situ regeneration of W armored PFCs via LMD-w.

CRediT authorship contribution statement

Jannik Tweer: Writing – original draft, Methodology, Investigation, Formal analysis, Data curation, Conceptualization. **Thomas Derra:** Writing – review & editing, Resources. **Daniel Dorow-Gerspach:** Writing – review & editing, Supervision, Conceptualization. **Mauricio Gago:** Writing – review & editing. **Sascha Gierlings:** Writing – review & editing, Resources. **Stefan Gräfe:** Writing – review & editing, Resources. **Gerald Pintsuk:** Writing – review & editing, Resources. **Marius Wirtz:** Writing – review & editing. **Christian Linsmeier:** Writing – review & editing, Supervision, Resources. **Thomas Bergs:** Writing – review & editing, Supervision, Resources. **Ghaleb Natour:** Writing – review & editing, Supervision, Resources.

Funding

This work has been carried out within the framework of the EUROfusion Consortium funded by the European Union via the Euratom research and training program (grant agreement no. 101052200—EUROfusion). The views and opinions expressed are, however, those of the authors only and do not necessarily reflect those of the European Union or the European Commission. Neither the European Union nor the European Commission can be held responsible for them.

Declaration of competing interest

The authors declare that they have no known competing financial interests or personal relationships that could have appeared to influence the work reported in this paper.

Acknowledgments

The author would like to thank: The colleagues from the Fraunhofer Institute for Production Technology for offering the opportunity to work at their facility. Wilfried Behr and Thomas Koppitz for brazing of the test components. Karsten Dominiczak and Andreas Weiß for their support in the HHF experiments. Gaby Esser for performing the profilometry scans. Noah Richter and Beatrix Göths for assistance in the mechanical preparation of the samples.

Data availability

Data will be made available on request.

References

[1] G. Federici, et al., Plasma-material interactions in current tokamaks and their implications for next step fusion reactors, (in English), Nucl. Fusion 41 (12r) (2001) 1967–2137, https://doi.org/10.1088/0029-5515/41/12/218.
[2] K. Krieger *et al.*, Scrape-off layer and divertor physics: Chapter 5 of the special issue: on the path to tokamak burning plasma operation, *Nuclear Fusion,* vol. 65, no. 4, p. 043001, 2025, https://doi.org/10.1088/1741-4326/adaf42.
[3] J. Linke *et al.*, Challenges for plasma-facing components in nuclear fusion, *Matter and Radiation at Extremes,* vol. 4, no. 5, 2019, https://doi.org/10.1063/1.5090100.
[4] Y. Ueda *et al.*, Baseline high heat flux and plasma facing materials for fusion, *Nuclear Fusion,* vol. 57, no. 9, Sep 2017, https://doi.org/10.1088/1741-4326/aa6b60.
[5] R.A. Pitts, et al., Physics conclusions in support of ITER W divertor monoblock shaping, (in English), Nucl. Mater. Energy 12 (2017) 60–74, https://doi.org/10.1016/j.nme.2017.03.005.
[6] M. Merola, F. Escourbiac, R. Raffray, P. Chappuis, T. Hirai, A. Martin, Overview and status of ITER internal components, Fusion Eng. Des. 89 (7–8) (2014) 890–895, https://doi.org/10.1016/j.fusengdes.2014.01.055.
[7] P.T. Lang, et al., ELM control strategies and tools: status and potential for ITER, (in English), Nucl. Fusion 53 (4) (2013), https://doi.org/10.1088/0029-5515/53/4/043004.
[8] A. Loarte *et al.*, Chapter 4: Power and particle control, *Nuclear Fusion,* vol. 47, no. 6, pp. S203-S263, 2007, https://doi.org/10.1088/0029-5515/47/6/s04.
[9] T.R. Barrett, et al., Progress in the engineering design and assessment of the European DEMO first wall and divertor plasma facing components, Fusion Eng. Des. 109–111 (2016) 917–924, https://doi.org/10.1016/j.fusengdes.2016.01.052.
[10] M. Wirtz, *Thermal shock behaviour of different tungsten grades under varying conditions*. Jülich: Forschungszentrum Jülich GmbH, Zentralbibliothek Verlag, 2012.
[11] R.A. Causey, J.N. Brooks, G. Federici, Tritium inventory and recovery in next-step fusion devices, (in English), Fusion Eng. Des. 61–62 (2002) 525–536, https://doi.org/10.1016/S0920-3796(02)00248-X.
[12] E. S. Lassner and W. D. Schubert, Tungsten: Properties, Chemistry, Technology of the Element, Alloys, and Chemical Compound, vol. 1st ed., 1999, https://doi.org/10.1007/978-1-4615-4907-9.
[13] V. Philipps, Tungsten as material for plasma-facing components in fusion devices, (in English), J. Nucl. Mater. 415 (1) (2011) S2–S9, https://doi.org/10.1016/j.jnucmat.2011.01.110.
[14] Y. Ueda, et al., Research status and issues of tungsten plasma facing materials for ITER and beyond, Fusion Eng. Des. 89 (7–8) (2014) 901–906, https://doi.org/10.1016/j.fusengdes.2014.02.078.
[15] J.N. Brooks, L. El-Guebaly, A. Hassanein, T. Sizyuk, Plasma-facing material alternatives to tungsten, Nucl. Fusion 55 (4) (2015) 043002, https://doi.org/10.1088/0029-5515/55/4/043002.
[16] Y. Noguchi, M. Saito, T. Maruyama, N. Takeda, Design progress of ITER blanket remote handling system towards manufacturing, Fusion Eng. Des. 136 (2018) 722–728, https://doi.org/10.1016/j.fusengdes.2018.03.068.
[17] T. Maruyama, A. Aburadani, N. Takeda, S. Kakudate, M. Nakahira, A. Tesini, Robot vision system R&D for ITER blanket remote-handling system, Fusion Eng. Des. 89 (9–10) (2014) 2404–2408, https://doi.org/10.1016/j.fusengdes.2014.01.004.

[18] J. Palmer, et al., The design and development of divertor remote handling equipment for ITER, Fusion Eng. Des. 82 (15–24) (2007) 1977–1982, https://doi.org/10.1016/j.fusengdes.2007.05.073.
[19] S. Sanders, G. Pegman, Remote operations for fusion using teleoperation, Ind. Robot Int. J. 33 (3) (2006) 174–177, https://doi.org/10.1108/01439910610659088.
[20] J.H. You, et al., Divertor of the European DEMO: Engineering and technologies for power exhaust, (in English), Fusion Eng. Des. 175 (2022), https://doi.org/10.1016/j.fusengdes.2022.113010.
[21] M. Li, J.-H. You, Interpretation of the deep cracking phenomenon of tungsten monoblock targets observed in high-heat-flux fatigue tests at 20 MW/m 2, Fusion Eng. Des. 101 (2015) 1–8, https://doi.org/10.1016/j.fusengdes.2015.09.008.
[22] T. DebRoy, et al., Additive manufacturing of metallic components – Process, structure and properties, Prog. Mater Sci. 92 (2018) 112–224, https://doi.org/10.1016/j.pmatsci.2017.10.001.
[23] D.G. Ahn, Directed energy deposition (DED) process: state of the art, Int. J. Precis. Eng. Manuf. Green Technol. 8 (2) (2021) 703–742, https://doi.org/10.1007/s40684-020-00302-7.
[24] A. Dass and A. Moridi, State of the Art in Directed Energy Deposition: From Additive Manufacturing to Materials Design, *Coatings*, vol. 9, no. 7, https://doi.org/10.3390/coatings9070418.
[25] R.M. Mahamood, E.T. Akinlabi, Processing parameters optimization for material deposition efficiency in laser metal deposited titanium alloy, Lasers Manuf. Mater. Process. 3 (1) (2016) 9–21, https://doi.org/10.1007/s40516-015-0020-5.
[26] M. Gipperich *et al.*, Reflectometry-based investigation of temperature fields during dual-beam Laser Metal Deposition, in *Laser 3D Manufacturing VIII*, 2021, https://doi.org/10.1117/12.2576112.
[27] M. Bambach, I. Sizova, F. Silze, M. Schnick, Comparison of laser metal deposition of Inconel 718 from powder, hot and cold wire, Proc. CIRP 74 (2018) 206–209, https://doi.org/10.1016/j.procir.2018.08.095.
[28] T. Bergs, S. Kammann, G. Fraga, J. Riepe, K. Arntz, Experimental investigations on the influence of temperature for Laser Metal Deposition with lateral Inconel 718 wire feeding, Proc. CIRP 94 (2020) 29–34, https://doi.org/10.1016/j.procir.2020.09.007.
[29] J. Tweer, et al., Initial experiments to regenerate the surface of plasma-facing components by wire-based laser metal deposition, Nucl. Mater. Energy 38 (2024), https://doi.org/10.1016/j.nme.2023.101577.
[30] J. Tweer, et al., Repair of heat load damaged plasma–facing material using the wire-based laser metal deposition process, Nucl. Mater. Energy 41 (2024) 101787, https://doi.org/10.1016/j.nme.2024.101787.
[31] J. Tweer, et al., Initial experiments to regenerate the surface of plasma-facing components by wire-based laser metal deposition, Nucl. Mater. Energy 38 (2024) 101577, https://doi.org/10.1016/j.nme.2023.101577.
[32] T. Loewenhoff, *Combined Steady State and High Cycle Transient Heat Load Simulation with the Electron Beam Facility JUDITH 2*. Jülich: Forschungszentrum Jülich GmbH, Zentralbibliothek Verlag, 2012.
[33] A. Schmidt *et al.*, First demonstration of non-destructive tests on tungsten-coated JET divertor CFC tiles in the electron beam facility JUDITH-2, *Physica Scripta,* vol. 2009, no. T138, p. 014034, 2009/12/30 2009, https://doi.org/10.1088/0031-8949/2009/T138/014034.
[34] P. Majerus, R. Duwe, T. Hirai, W. Kühnlein, J. Linke, M. Rödig, The new electron beam test facility JUDITH II for high heat flux experiments on plasma facing components, Fusion Eng. Des. 75–79 (2005) 365–369, https://doi.org/10.1016/j.fusengdes.2005.06.058.
[35] T. Hirai, et al., ITER tungsten divertor design development and qualification program, Fusion Eng. Des. 88 (9) (2013) 1798–1801, https://doi.org/10.1016/j.fusengdes.2013.05.010.
[36] R.A. Pitts, et al., Status and physics basis of the ITER divertor, (in English), Phys. Scr. T138 (2009), https://doi.org/10.1088/0031-8949/2009/T138/014001.
[37] G. Pintsuk, I. Bobin-Vastra, S. Constans, P. Gavila, M. Rödig, B. Riccardi, Qualification and post-mortem characterization of tungsten mock-ups exposed to cyclic high heat flux loading, Fusion Eng. Des. 88 (9) (2013) 1858–1861, https://doi.org/10.1016/j.fusengdes.2013.05.091.
[38] E. Visca, S. Libera, A. Mancini, G. Mazzone, A. Pizzuto, C. Testani, Hot radial pressing: an alternative technique for the manufacturing of plasma-facing components, Fusion Eng. Des. 75–79 (2005) 485–489, https://doi.org/10.1016/j.fusengdes.2005.06.123.
[39] D. W. Hahn and M. N. Özişik, Heat Conduction Fundamentals, in *Heat Conduction*: John Wiley & Sons, Inc., 2012, pp. 1-39.
[40] M. Siddique, A.-R.-A. Khaled, N.I. Abdulhafiz, A.Y. Boukhary, Recent advances in heat transfer enhancements: a review report, Int. J. Chem. Eng. 2010 (1) (2010) 106461, https://doi.org/10.1155/2010/106461.
[41] B. S. Petukhov, Heat Transfer and Friction in Turbulent Pipe Flow with Variable Physical Properties, in *Advances in Heat Transfer*, vol. 6, J. P. Hartnett and T. F. Irvine Eds.: Elsevier, 1970, pp. 503-564.
[42] E.N. Sieder, G.E. Tate, Heat transfer and pressure drop of liquids in tubes, Ind. Eng. Chem. 28 (12) (1936) 1429–1435.
[43] S. Hall, 12 - Closed Loop Heat Transfer Systems, in *Branan's Rules of Thumb for Chemical Engineers (Fifth Edition)*, S. Hall Ed. Oxford: Butterworth-Heinemann, 2012, pp. 203–219.
[44] Y. Bournonville, M. Grandotto, S. Pascal-Ribot, P. Spitz, F. Escourbiac, Numerical simulation of swirl-tube cooling concept, application to the ITER project, Fusion Eng. Des. 84 (2) (2009) 501–504, https://doi.org/10.1016/j.fusengdes.2008.11.028.
[45] T. Loewenhoff, T. Hirai, S. Keusemann, J. Linke, G. Pintsuk, A. Schmidt, Experimental simulation of Edge Localised Modes using focused electron beams – features of a circular load pattern, J. Nucl. Mater. 415 (2011) S51–S54, https://doi.org/10.1016/j.jnucmat.2010.08.065.
[46] J. Linke *et al.*, Performance of different tungsten grades under transient thermal loads, *Nuclear Fusion,* vol. 51, no. 7, 2011, https://doi.org/10.1088/0029-5515/51/7/073017.
[47] M. Wirtz, J. Linke, T. Loewenhoff, G. Pintsuk, I. Uytdenhouwen, Transient heat load challenges for plasma-facing materials during long-term operation, Nucl. Mater. Energy 12 (2017) 148–155, https://doi.org/10.1016/j.nme.2016.12.024.
[48] N. Ghanadi and S. Pasebani, A Review on Wire-Laser Directed Energy Deposition: Parameter Control, Process Stability, and Future Research Paths, *Journal of Manufacturing and Materials Processing*, vol. 8, no. 2, https://doi.org/10.3390/jmmp8020084.
[49] W. Jia, et al., Influence of energy area densities on microstructure evolution and properties of laser direct energy deposited Ni-Co-Mn-Al-Y magnetic shape memory alloy, Addit. Manuf. 60 (2022) 103232, https://doi.org/10.1016/j.addma.2022.103232.
[50] M. Gipperich, J. Riepe, R. Day, and T. Bergs, Express Wire Coil Cladding (EW2C) As an Advanced Technology To Accelerate Additive Manufacturing and Coating, in *ASME Turbo Expo 2021: Turbomachinery Technical Conference and Exposition*, 2021, vol. Volume 7: Industrial and Cogeneration; Manufacturing Materials and Metallurgy, V007T17A001, https://doi.org/10.1115/gt2021-58709.
[51] J. Linke, P. Lorenzetto, P. Majerus, M. Merola, D. Pitzer, M. Rödig, EU development of high heat flux components, (in English), Fusion Sci. Technol. 47 (3) (2005) 678–685, https://doi.org/10.13182/Fst05-A764.
[52] M. Becoulet, et al., Edge localized modes control:: experiment and theory, (in English), J. Nucl. Mater. 337 (1–3) (2005) 677–683, https://doi.org/10.1016/j.jnucmat.2004.09.074.
[53] T. Hirai, G. Pintsuk, Thermo-mechanical calculations on operation temperature limits of tungsten as plasma facing material, Fusion Eng. Des. 82 (4) (2007) 389–393, https://doi.org/10.1016/j.fusengdes.2007.03.032.
[54] E.S. Gadelmawla, M.M. Koura, T.M.A. Maksoud, I.M. Elewa, H.H. Soliman, Roughness parameters, J. Mater. Process. Technol. 123 (1) (2002) 133–145, https://doi.org/10.1016/S0924-0136(02)00060-2.
[55] J.V. Gordon, et al., Defect structure process maps for laser powder bed fusion additive manufacturing, Addit. Manuf. 36 (2020), https://doi.org/10.1016/j.addma.2020.101552.
[56] Z. Sun, et al., Post examination of tungsten monoblocks subjected to high heat flux tests of ITER full-tungsten divertor qualification program, Fusion Eng. Des. 121 (2017) 60–69, https://doi.org/10.1016/j.fusengdes.2017.06.009.
[57] S. Panayotis, et al., Fracture modes of ITER tungsten divertor monoblock under stationary thermal loads, Fusion Eng. Des. 125 (2017) 256–262, https://doi.org/10.1016/j.fusengdes.2017.08.009.
[58] G. Pintsuk, et al., Characterization of ITER tungsten qualification mock-ups exposed to high cyclic thermal loads, Fusion Eng. Des. 98–99 (2015) 1384–1388, https://doi.org/10.1016/j.fusengdes.2015.01.037.
[59] T. Hirai, et al., Status of technology R&D for the ITER tungsten divertor monoblock, J. Nucl. Mater. 463 (2015) 1248–1251, https://doi.org/10.1016/j.jnucmat.2014.12.027.
[60] P. Gavila, B. Riccardi, G. Pintsuk, G. Ritz, V. Kuznetsov, A. Durocher, High heat flux testing of EU tungsten monoblock mock-ups for the ITER divertor, Fusion Eng. Des. 98–99 (2015) 1305–1309, https://doi.org/10.1016/j.fusengdes.2014.12.006.
[61] M. Wirtz, J. Linke, T. Loewenhoff, G. Pintsuk, I. Uytdenhouwen, Thermal shock tests to qualify different tungsten grades as plasma facing material, Phys. Scr. T167 (2016), https://doi.org/10.1088/0031-8949/t167/1/014015.
[62] A. Kapoustina, T. Hirai, J. Linke, M. Rödig, Detection of heat transfer properties of CFC-plasma facing components by IR-observation and high heat flux testing, Phys. Scr. 2004 (T111) (2004) 181, https://doi.org/10.1238/Physica.Topical.111a00181.
[63] G. Pintsuk, et al., Long-pulse high heat flux testing of tungsten monoblock target mock-ups for investigation of creep fatigue interaction, Nucl. Mater. Energy 39 (2024) 101687, https://doi.org/10.1016/j.nme.2024.101687.
[64] Y. Corre, et al., Testing of ITER-grade plasma facing units in the WEST tokamak: Progress in understanding heat loading and damage mechanisms, Nucl. Mater. Energy 37 (2023) 101546, https://doi.org/10.1016/j.nme.2023.101546.

[65] A. Eksaeva, et al., The impact of surface morphology on the erosion of metallic surfaces – Modelling with the 3D Monte-Carlo code ERO2.0, Nucl. Mater. Energy 27 (2021,) 100987, https://doi.org/10.1016/j.nme.2021.100987.
[66] Y. Corre, et al., Plasma exposure of a pre-damaged ITER-like plasma facing unit in the WEST tokamak: in-situ and post-mortem measurements, Nucl. Mater. Energy 34 (2023) 101366, https://doi.org/10.1016/j.nme.2023.101366.
[67] T. Loewenhoff, S. Antusch, G. Pintsuk, M. Rieth, M. Wirtz, High pulse number thermal shock testing of tungsten alloys produced by powder injection molding, Nucl. Mater. Energy 20 (2019) 100680, https://doi.org/10.1016/j.nme.2019.100680.
[68] A.S. Arakcheev, et al., Theoretical investigation of crack formation in tungsten after heat loads, J. Nucl. Mater. 463 (2015) 246–249, https://doi.org/10.1016/j.jnucmat.2014.10.090.
[69] T. Pütterich *et al.*, Calculation and experimental test of the cooling factor of tungsten, (in English), *Nuclear Fusion,* vol. 50, no. 2, Feb 2010, https://doi.org/10.1088/0029-5515/50/2/025012.
[70] L. Singheiser, T. Hirai, J. Linke, G. Pintsuk, M. Rödig, Plasma-facing materials for thermo-nuclear fusion devices, T Indian I Met. 62 (2) (2009) 123–128, https://doi.org/10.1007/s12666-009-0016-y.
[71] J.H. You, H. Greuner, B. Böswirth, K. Hunger, S. Roccella, H. Roche, High-heat-flux performance limit of tungsten monoblock targets: Impact on the armor materials and implications for power exhaust capacity, Nucl. Mater. Energy 33 (2022) 101307, https://doi.org/10.1016/j.nme.2022.101307.
[72] S.-H. Pan, et al., Additive manufacturing of tungsten, tungsten-based alloys, and tungsten matrix composites, Tungsten 5 (1) (2022) 1–31, https://doi.org/10.1007/s42864-022-00153-6.
[73] A. v. Müller *et al.*, Progress in additive manufacturing of pure tungsten for plasma-facing component applications, *Journal of Nuclear Materials,* vol. 566, Aug 1 2022, https://doi.org/10.1016/j.jnucmat.2022.153760.
[74] D. Dorow-Gerspach, A. Kirchner, T. Loewenhoff, G. Pintsuk, T. Weißgärber, M. Wirtz, Additive manufacturing of high density pure tungsten by electron beam melting, Nucl. Mater. Energy 28 (2021), https://doi.org/10.1016/j.nme.2021.101046.
[75] A.V. Müller, et al., Additive manufacturing of pure tungsten by means of selective laser beam melting with substrate preheating temperatures up to 1000°C, Nucl. Mater. Energy 19 (2019) 184–188, https://doi.org/10.1016/j.nme.2019.02.034.